1996ApJ...461..424O

THE ASTROPHYSICAL JOURNAL, 461:424–444, 1996 April 10
© 1996. The American Astronomical Society. All rights reserved. Printed in U.S.A.

# MAGNETOHYDRODYNAMIC WAVES IN SOLAR CORONAL ARCADES

R. OLIVER,[1] A. W. HOOD, AND E. R. PRIEST
Mathematical and Computational Sciences Department, University of St. Andrews, St Andrews KY16 9SS, Scotland, UK
*Received 1995 March 14; accepted 1995 October 19*

## ABSTRACT

The propagation of magnetohydrodynamic (MHD) disturbances in a solar coronal arcade is investigated. The equations of magnetoacoustic fast and slow waves are presented in a very general form: a pair of second-order, two-dimensional partial differential equations in which the two dependent variables are the components of the velocity perturbation parallel and normal to the magnetic field. In deriving these equations, a general two-dimensional equilibrium structure with no longitudinal magnetic field component has been assumed. Thus, the equations are valid for rather general configurations. Alfvén waves are decoupled from the magnetoacoustic modes and give rise to an Alfvén continuous spectrum.

The solutions to the wave equations have been obtained numerically, and the perturbed restoring forces (plasma pressure gradient, magnetic pressure gradient, and magnetic tension), responsible for the oscillatory modes, have also been computed. These forces give rise to the propagation of MHD waves, and their interaction determines the physical properties of the various modes. Therefore, the spatial structure of the forces and their interplay are basic in characterizing fast and slow modes.

Pure fast and pure slow waves do not exist in the present configuration, although for the considered parameter values, all modes possess either fast-mode or slow-mode properties. "Slow" modes in these two-dimensional equilibria can propagate across the magnetic field only with difficulty and so display a structure of bands, centred about certain field lines, of alternate positive and negative parallel velocity component. On the other hand, "fast" modes are isotropic in nature, and their spatial structure is not so intimately linked to the shape of field lines. In addition, as a consequence of the distinct characteristic propagation speeds of fast and slow modes, their frequencies typically differ by an order of magnitude.

*Subject headings:* MHD — Sun: corona — waves

## 1. INTRODUCTION

The physical structure of the solar corona is very complicated. The interaction between the magnetic field and the plasma plays a central role in the physical properties of this medium and is responsible for many phenomena occurring in the corona. Key subjects in this context are, among others, the equilibria and slow time evolution of different types of structure (loops, arcades, prominences, etc.), the propagation and nature of waves, and the heating of the plasma to a few million degrees. All of them are mutually connected, and physical interpretations to the questions that arise need to be given.

A possible path is to consider well-defined coronal structures and to derive some of their intrinsic features by comparing observed frequencies of oscillation with the values predicted from theoretical modeling, an approach which we may refer to as *coronal seismology*. Apparently, this requires a previous knowledge of the quantities one wants to determine, although a rough physical idea of the equilibrium variables of the structure under study can be enough. On the other hand, different configurations of magnetic field and plasma can be reasonably expected to possess different frequencies of oscillation. In this sense, the dispersion diagram can be thought of as being a kind of signature or "fingerprint" of a given coronal object. Once a given structure in the corona has been identified, one should be able to select among all equilibrium models the one whose dispersion diagram best fits the observed frequencies. Further improvement and comparison of theoretical and observational results then allows one to improve this basic equilibrium model by inferring more precisely the magnetic field configuration and plasma properties. Hopefully, the end product of this process, similar in its aim and means to that of helioseismology, is a better understanding of the physical processes occurring in the solar corona.

A coronal arcade of magnetic field lines in which the magnetic Lorentz force is in balance with the pressure gradient is considered here. Coronal arcades have been known for a very long time and are routinely observed in X-rays (e.g., Acton et al. 1992). They may be formed as the magnetic field reconnects behind an outward moving magnetic eruption and, once created, these arcades usually remain as stable objects for days or weeks. It is during this stage of their existence that arcades can be subject to a seismic study. One of these objects can be set into motion by a disturbance coming from a flare and can continue oscillating in one or more of its normal modes.

The problem of standing magnetohydrodynamic (MHD) waves in such a system is investigated in this paper. A few assumptions are made in order to simplify the wave equations while not losing too much of the physical details of the real problem. An important simplification is the decoupling of the Alfvén wave from the fast and slow magnetoacoustic modes, which are studied separately. One of the main aims of this paper is the investigation of the influence of a nonpotential, two-dimensional equilibrium on these modes. The equations governing magnetoacoustic waves are cast here as a pair of coupled partial differential equations for the components of the oscillatory velocity parallel and normal to the magnetic field and are solved numerically by means of finite differences.

[1] On leave from Departament de Física, Universitat de les Illes Balears, 07071 Palma de Mallorca, Spain (present address).



© American Astronomical Society • Provided by the NASA Astrophysics Data System

1996ApJ...461..424O



A point of capital importance is the boundary conditions. The arcade is like a column of material extending over the photosphere and embedded in the corona. For simplicity, we regard the system as shielded from any influence from the rest of the corona, i.e., it is assumed that no material traverses the lateral boundaries of the arcade which results in simple conditions on the unknowns. Moreover, all perturbations are assumed to vanish at infinite height. One also has to deal with the influence of the heavy photospheric plasma on the vibrations of the arcade, which has been the subject of debate over the last decade. Two sets of ideal MHD boundary conditions, which assume the vanishing of the velocity component normal to the magnetic field at the photospheric level, have been commonly used: rigid wall (e.g., Kuperus & Raadu 1974; Rosner, Low, & Holzer 1986) and flow-through conditions (e.g., Einaudi & Van Hoven 1981). The difference between them is that rigid wall conditions require the vanishing of all velocity components, whereas flow-through conditions allow for a flow along magnetic field lines. Van der Linden, Hood, & Goedbloed (1994) studied the influence of photospheric gravitational stratification on the ideal MHD stability and modes of coronal magnetic structures and concluded that rigid wall conditions mimic the field line anchoring produced by the dense photosphere better than flow-through conditions. Even more, the modeling of the photospheric influence by rigid wall boundary conditions gives good approximations to those frequencies which are much larger than the photospheric Alfvén timescale because the photosphere cannot react to high-frequency disturbances incident upon it.

For a general description of the subject of MHD waves, the reader is referred to reviews and papers both in the context of space plasmas (e.g., Goossens 1991; Roberts 1985, 1991) and in the context of laboratory plasmas (e.g., Goedbloed 1975). It is worth referring to a related problem considered by Goedbloed & Halberstadt (1994), who studied a coronal loop modeled as a slab of plasma threaded by an oblique magnetic field. The system is line-tied at its ends and periodic in one direction to simulate the azimuthal periodicity. One important conclusion of this work is that the line-tying effect completely changes the character of the MHD modes, which cannot be pure fast, slow, or Alfvén modes except in certain limits. In general, the modes of the system present mixed properties and consist of Alfvén, fast, and slow components. In the limit of straight magnetic field, more akin to the unsheared magnetic configuration considered in this paper, one obtains an Alfvén branch of pure modes decoupled from the magnetoacoustic branch, which exhibits mode coupling.

Another work worth mentioning is that by Oliver et al. (1993), in which the fast normal modes of a potential arcade, with a background plasma in hydrostatic equilibrium, are studied. Their configuration with the parameter value $\delta = 0$ ($\delta$ being the ratio of the magnetic scale height to the pressure scale height) corresponds to the absence of gravity and coincides with a limiting case of the equilibrium used in this paper. Thus, we will use the results in Oliver et al. (1993) to investigate the effects of relaxing the potential assumption on the oscillatory modes of the system. In addition, the influence of pressure forces on the fast mode will also be investigated.

The plan of the paper is as follows. The basic equations are given in § 2: the nonpotential arcade equilibrium structure is described first; next, the equations for adiabatic MHD waves are developed and expressed in such a way as to make them appropriate for their numerical solution; from these equations, the expressions governing the slow and Alfvén continua in the present model are also determined. The numerical procedure for the solution of the magnetoacoustic modes is explained briefly in § 3. The problem reduces to solving an algebraic eigenvalue system which can be tackled using standard techniques. Section 4 is devoted to the study of the slow and Alfvén continua, and the results obtained serve as a first check of the two-dimensional numerical code developed in § 3. In § 5 the influence of the two-dimensional, nonpotential equilibrium on magnetoacoustic modes is addressed. Finally, in § 6 the conclusions are drawn.

## 2. BASIC EQUATIONS

### 2.1. *Equilibrium Configuration*

An arcade of magnetic field lines is considered which is in mechanical equilibrium under a balance between the Lorentz force and the pressure gradient, namely,

$$\frac{1}{\mu}(\nabla \times \boldsymbol{B}) \times \boldsymbol{B} - \nabla p = 0 \,. \tag{1}$$

In finding a solution to this equation, it is assumed that the variations in the $y$-direction, the direction of the arcade axis, are negligible, which renders the pressure uniform on each magnetic surface and allows one to write the magnetic field as $\boldsymbol{B} = \nabla A \times \hat{e}_y + B_y(A)\hat{e}_y$, where $A(x, z)$ is the magnetic flux function. We assume further that the magnetic field has no shear and take

$$\boldsymbol{B} = \nabla A \times \hat{e}_y \,. \tag{2}$$

This simplification restricts the generality of the equilibrium, but it is useful in reducing the complexity of the oscillatory spectrum of the system.

Equation (1) can now be cast as

$$-\nabla p = \frac{1}{\mu}(\nabla^2 A)\nabla A \,, \tag{3}$$

which results in the pressure being expressed in terms of the flux function. A particular solution to this equation (see Priest 1988) is obtained by setting

$$\nabla^2 A = (l^2 - k^2)A \,, \tag{4}$$

© American Astronomical Society • Provided by the NASA Astrophysics Data System

1996ApJ...461..426



and integrating equation (3) gives

$$p(A) = (k^2 - l^2)\frac{A^2}{2\mu} + p_0 , \tag{5}$$

with $l$, $k$, and $p_0$ positive constants.

We adopt the following solution to equation (4):

$$A(x, z) = \frac{B_0}{k}\cos kx e^{-lz} . \tag{6}$$

Direct substitution of this expression into equations (2) and (5) gives the magnetic field components

$$B_x(x, z) = B_0\frac{l}{k}\cos kx e^{-lz} , \tag{7}$$

$$B_z(x, z) = -B_0 \sin kx e^{-lz} , \tag{8}$$

and the pressure distribution

$$p(x, z) = \frac{B_0^2}{2\mu}\left[\left(1 - \frac{l^2}{k^2}\right)\cos^2 kx e^{-2lz} + \beta_0\right], \tag{9}$$

where

$$\beta_0 = \frac{2\mu p_0}{B_0^2} \tag{10}$$

is another free parameter of the equilibrium. The coordinate system has been chosen so that the $y$-axis is parallel to the ignorable direction of the arcade, the $z$-axis is vertical, and the $x$-axis is horizontal. The magnetic configuration is periodic in the $x$-direction, with a periodicity length $2L = \pi/k$ (see Fig. 1*a*).

Another important physical variable is the plasma $\beta$,

$$\beta(x, z) = \frac{2\mu p}{B^2} = \frac{(k^2/l^2)\beta_0 e^{2lz} - [1 - (k^2/l^2)]\cos^2 kx}{(k^2/l^2) + [1 - (k^2/l^2)]\cos^2 kx} . \tag{11}$$

It is worthwhile noticing that for $\beta$ to be positive everywhere it is necessary to require

$$1 + \beta_0 > \left(\frac{l}{k}\right)^2 , \tag{12}$$

and so not all values of the parameters $l/k$ and $\beta_0$ yield physically acceptable equilibria. The quantity $\beta_0 = \beta(x = \pm L, z = 0)$ is the minimum of the plasma $\beta$.

The temperature and density are linked to each other and to the pressure by the perfect gas law

$$p = \frac{\rho RT}{\tilde{\mu}} . \tag{13}$$

Thus, we can either impose the temperature profile or the density profile and then calculate the other by eliminating $p$ from equations (9) and (13).

Apart from this choice, one also needs to impose the value of two other parameters, namely, $\beta_0$ and $l/k$, which have to be restricted to a certain range to have an equilibrium in which the plasma $\beta$ does not reach too high values. Moreover, the exponential term dominates the vertical variation of $\beta$ in equation (11), and it is necessary to restrict the height of the system to a maximum value $z = H$ if $\beta$ is to be kept small. We will mostly consider $H = L$, which corresponds to an arcade whose height is equal to half its width. For $10^{-3} \leq \beta_0 \leq 10^{-2}$ and $0.9 \leq l/k \leq 1.0$, the beta of the plasma is always below 0.5, and so $\beta_0$ and $l/k$ will be taken within those ranges in most of the computations. Higher values of $\beta_0$ combined with lower values of $l/k$ yield larger values of $\beta$.

One should be aware of the fact that in this equilibrium the plasma beta increases without bound in the vertical direction, contrary to what one expects in the corona. This is a consequence of excluding the gravitational term from equation (1), which together with equation (4) gives rise to an equilibrium magnetic field that goes to zero and a pressure that remains constant as $z \to \infty$. Obviously, gravity should be included in the determination of the equilibrium structure, since the total height of a coronal arcade will usually be of the order of or longer than the pressure scale height. The MHD modes of the arcade would then be driven by three restoring forces: the pressure gradient, the magnetic Lorentz force, and gravity. In this paper, we want to concentrate on the interplay between the first two of these forces, so gravity is not introduced in our calculations.

### 2.2. *Equations of MHD Waves*

In this section, the equations of linear, ideal MHD waves are derived for a general two-dimensional equilibrium without gravity and with no longitudinal component of the magnetic field. Thus, instead of taking $\boldsymbol{B}$ and $p$ as given by expressions (7), (8), and (9), only equations (1) and (2) are used.

© American Astronomical Society • Provided by the NASA Astrophysics Data System

1996ApJ...461..424O

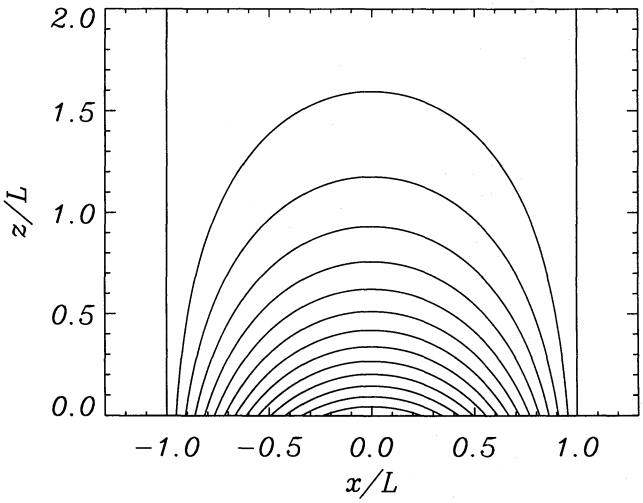


FIG. 1a

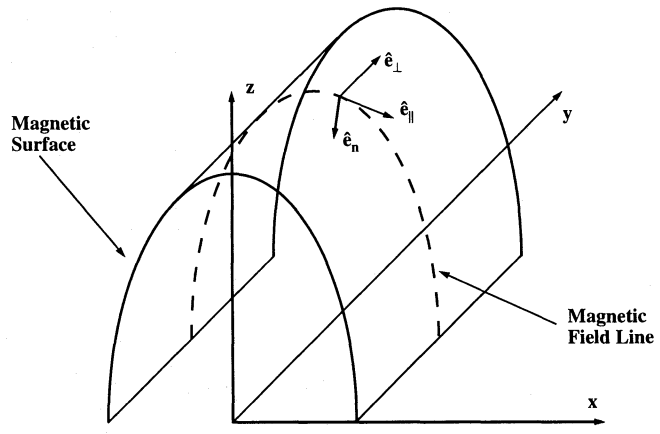


FIG. 1b

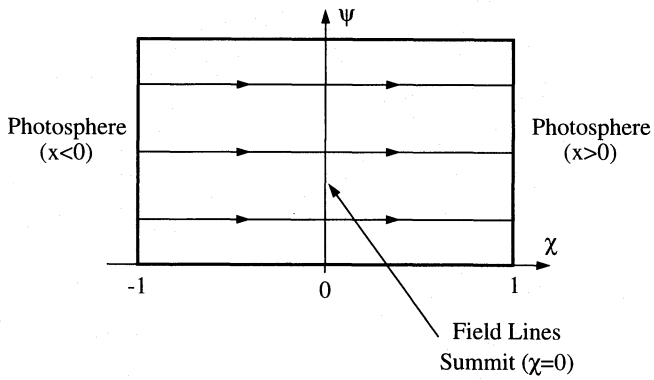


FIG. 1c

FIG. 1.—(*a*) Equilibrium magnetic configuration for $l/k = 0.95$. (*b*) Sketch of a magnetic surface with the field-related vectors $\hat{e}_n$, $\hat{e}_\parallel$, and $\hat{e}_\perp \equiv \hat{e}_y$. (*c*) Sketch of the arcade region in flux coordinates, where magnetic field lines are lines of constant $\psi$, emerging through the photosphere at $\chi = -1$ and submerging in at $\chi = 1$.

The physical variables are assumed to suffer small displacements from their equilibrium values. The system is then set into an oscillatory state, which is described by the linearized equations of mass continuity, energy (for adiabatic changes of state), induction, and momentum. Assuming time variations of the form $\exp(i\omega t)$, these four equations can be cast as follows:

$$i\omega\rho_1 = -\boldsymbol{v}\cdot\nabla\rho - \rho\nabla\cdot\boldsymbol{v}\,, \tag{14}$$

$$i\omega p_1 = -\boldsymbol{v}\cdot\nabla p - \gamma p\nabla\cdot\boldsymbol{v}\,, \tag{15}$$

$$i\omega\boldsymbol{B}_1 = \nabla\times(\boldsymbol{v}\times\boldsymbol{B})\,, \tag{16}$$

and

$$i\omega\rho\boldsymbol{v} = -\nabla p_1 + \frac{1}{\mu}(\nabla\times\boldsymbol{B})\times\boldsymbol{B}_1 + \frac{1}{\mu}(\nabla\times\boldsymbol{B}_1)\times\boldsymbol{B} = -\nabla p_1 - \nabla p_{1m} + \mathcal{T}_1\,, \tag{17}$$

with $\rho_1$, $p_1$, and $\boldsymbol{B}_1$ the density, pressure, and magnetic field perturbations. The equation of mass continuity, from which the perturbation to the equilibrium density can be obtained, is not needed since this variable is not present in the other equations and is only given for future reference. Moreover, in equation (17) the perturbed Lorentz force has been written as the sum of the gradient of the perturbed magnetic pressure ($p_{1m}$) and the perturbed magnetic tension ($\mathcal{T}_1$), which are defined as

$$p_{1m} = \frac{\boldsymbol{B}\cdot\boldsymbol{B}_1}{\mu}\,, \tag{18}$$

$$\mathcal{T}_1 = \frac{1}{\mu}(\boldsymbol{B}\cdot\nabla)\boldsymbol{B}_1 + \frac{1}{\mu}(\boldsymbol{B}_1\cdot\nabla)\boldsymbol{B}\,. \tag{19}$$

At this point, the basis vectors that will be used to project the various vectors are selected. It will later prove advantageous, for a better understanding of the results, to decompose all vectors in equations (14), (15), (16), and (17) into their normal, parallel, and perpendicular components (Fig. 1*b*). These three directions are defined at each point by the magnetic field, the

© American Astronomical Society • Provided by the NASA Astrophysics Data System

1996ApJ...461..428



normal to $\boldsymbol{B}$ parallel to the magnetic surface, and the normal to these two vectors, and so they are associated with the three orthonormal vectors

$$\hat{\boldsymbol{e}}_n = \frac{\nabla A}{B}\,, \tag{20}$$

$$\hat{\boldsymbol{e}}_{\parallel} = \frac{\boldsymbol{B}}{B}\,, \tag{21}$$

and

$$\hat{\boldsymbol{e}}_{\perp} = \hat{\boldsymbol{e}}_y\,. \tag{22}$$

In what follows, we simply replace the subscript "$\perp$" by "$y$" and refer to the perpendicular ($\perp$) direction as the $y$-direction. Thus, the velocity can be written as

$$\boldsymbol{v} = v_n \hat{\boldsymbol{e}}_n + v_{\parallel}\hat{\boldsymbol{e}}_{\parallel} + v_y \hat{\boldsymbol{e}}_y\,. \tag{23}$$

All other vectors, including the vector equations (16) and (17), can also be expressed as a linear combination of their $n$, $\parallel$, and $y$-components.

Another simplifying assumption is adopted here, namely, the independence of all perturbed quantities from $y$. In this way, the system of differential equations to be solved simplifies considerably by the decoupling of the Alfvén mode from the magnetoacoustic modes, as shown below.

Using the decomposition of the velocity in its field-related components (eq. [23]) and with $\partial/\partial y = 0$, the plasma pressure, magnetic field, and magnetic pressure perturbations can be written as

$$i\omega p_1 = -\gamma p \frac{1}{B}(\nabla A\cdot\nabla)v_n - \left[p_a + \gamma p\left(\frac{\nabla^2 A}{B} - B_a\right)\right]v_n - \gamma p \frac{1}{B}(\boldsymbol{B}\cdot\nabla)v_{\parallel} + \gamma p B_s v_{\parallel}\,, \tag{24}$$

$$i\omega \boldsymbol{B}_1 = B\left\{\left[\frac{1}{B}(\boldsymbol{B}\cdot\nabla)v_n + B_s v_n\right]\hat{\boldsymbol{e}}_n - \left[\frac{1}{B}(\nabla A\cdot\nabla)v_n + B_a v_n\right]\hat{\boldsymbol{e}}_{\parallel} + \frac{1}{B}(\boldsymbol{B}\cdot\nabla)v_y\hat{\boldsymbol{e}}_y\right\}, \tag{25}$$

and

$$i\omega p_{1m} = -\frac{B^2}{\mu}\left[\frac{1}{B}(\nabla A\cdot\nabla)v_n + B_a v_n\right]. \tag{26}$$

In deriving these formulae, the spatial derivatives have been written in terms of $\nabla A\cdot\nabla$ and $\boldsymbol{B}\cdot\nabla$. We have also used some vector identities and the equations for the divergence and the gradient that can be found in Appendix A, where the short-hand notation for some derivatives of $B$ and $p$ ($B_a$, $p_a$, etc.) is also given.

From equation (24), the pressure gradient term is given by

$$\begin{aligned}
-\frac{i\omega}{\rho}\nabla p_1 = {} & \left\{c_s^2\frac{1}{B^2}(\nabla A\cdot\nabla)^2 v_n + \left[(\gamma+1)\frac{p_a}{\rho} + c_s^2\left(\frac{\nabla^2 A}{B} - 2B_a\right)\right]\frac{1}{B}(\nabla A\cdot\nabla)v_n\right. \\
& + \left[\frac{\gamma p_a}{\rho}\left(\frac{\nabla^2 A}{B} - B_a\right) + \frac{c_s^2}{B}(\nabla A\cdot\nabla)\left(\frac{\nabla^2 A}{B} - B_a\right) + \frac{p_{aa}}{\rho}\right]v_n + c_s^2\frac{1}{B^2}(\nabla A\cdot\nabla)(\boldsymbol{B}\cdot\nabla)v_{\parallel} - c_s^2 B_s\frac{1}{B}(\nabla A\cdot\nabla)v_{\parallel} \\
& \left. + \left(\frac{\gamma p_a}{\rho} - c_s^2 B_a\right)\frac{1}{B}(\boldsymbol{B}\cdot\nabla)v_{\parallel} - \left[\frac{\gamma p_a}{\rho}B_s + c_s^2(B_{as} - 2B_a B_s)\right]v_{\parallel}\right\}\hat{\boldsymbol{e}}_n \\
& + \left\{c_s^2\frac{1}{B^2}(\boldsymbol{B}\cdot\nabla)(\nabla A\cdot\nabla)v_n - c_s^2 B_s\frac{1}{B}(\nabla A\cdot\nabla)v_n + \left[c_s^2\left(\frac{\nabla^2 A}{B} - B_a\right) + \frac{p_a}{\rho}\right]\frac{1}{B}(\boldsymbol{B}\cdot\nabla)v_n\right. \\
& \left. + \left[\frac{c_s^2}{B}(\boldsymbol{B}\cdot\nabla)\left(\frac{\nabla^2 A}{B} - B_a\right) + \frac{p_{sa}}{\rho}\right]v_n + c_s^2\frac{1}{B^2}(\boldsymbol{B}\cdot\nabla)^2 v_{\parallel} - 2c_s^2 B_s\frac{1}{B}(\boldsymbol{B}\cdot\nabla)v_{\parallel} - c_s^2(B_{ss} - 2B_s^2)v_{\parallel}\right\}\hat{\boldsymbol{e}}_{\parallel}\,.
\end{aligned} \tag{27}$$

From equation (26), the magnetic pressure term is

$$\begin{aligned}
-\frac{i\omega}{\rho}\nabla p_{1m} = {} & v_A^2\left[\frac{1}{B^2}(\nabla A\cdot\nabla)^2 v_n + 2B_a\frac{1}{B}(\nabla A\cdot\nabla)v_n + B_{aa}v_n\right]\hat{\boldsymbol{e}}_n \\
& + v_A^2\left[\frac{1}{B^2}(\boldsymbol{B}\cdot\nabla)(\nabla A\cdot\nabla)v_n + B_s\frac{1}{B}(\nabla A\cdot\nabla)v_n + B_a\frac{1}{B}(\boldsymbol{B}\cdot\nabla)v_n + B_{sa}v_n\right]\hat{\boldsymbol{e}}_{\parallel}\,.
\end{aligned} \tag{28}$$

© American Astronomical Society • Provided by the NASA Astrophysics Data System

1996ApJ...461..4240



And from equations (19) and (25), the magnetic tension term is given by

$$\frac{i\omega}{\rho}\mathcal{T}_1 = v_A^2\left\{\frac{1}{B^2}(\boldsymbol{B}\cdot\nabla)^2 v_n + 2\left(\frac{\nabla^2 A}{B} - B_a\right)\frac{1}{B}(\nabla A\cdot\nabla)v_n + \left[B_{ss} - 2B_s^2 + 2B_a\left(\frac{\nabla^2 A}{B} - B_a\right)\right]v_n\right\}\hat{\boldsymbol{e}}_n$$
$$+ v_A^2\left[-\frac{1}{B^2}(\boldsymbol{B}\cdot\nabla)(\nabla A\cdot\nabla)v_n - B_s\frac{1}{B}(\nabla A\cdot\nabla)v_n + \left(\frac{\nabla^2 A}{B} - B_a\right)\frac{1}{B}(\boldsymbol{B}\cdot\nabla)v_n\right.$$
$$\left. + \left(B_s\frac{\nabla^2 A}{B} - B_{sa}\right)v_n\right]\hat{\boldsymbol{e}}_\parallel + v_A^2\frac{1}{B^2}(\boldsymbol{B}\cdot\nabla)^2 v_y\,\hat{\boldsymbol{e}}_y\,. \tag{29}$$

The sound and Alfvén speeds are defined as

$$c_s^2 = \frac{\gamma RT}{\tilde{\mu}}\,, \tag{30}$$

$$v_A^2 = \frac{B^2}{\mu\rho} = \frac{2c_s^2}{\gamma\beta}\,. \tag{31}$$

These expressions are next inserted into the linearized momentum equation (17), which multiplied by $i\omega/\rho$ yields the components

$$-\omega^2 v_n = -\frac{i\omega}{\rho}(\nabla p_1)_n - \frac{i\omega}{\rho}(\nabla p_{1m})_n + \frac{i\omega}{\rho}\mathcal{T}_{1n}\,, \tag{32}$$

$$-\omega^2 v_\parallel = -\frac{i\omega}{\rho}(\nabla p_1)_\parallel - \frac{i\omega}{\rho}(\nabla p_{1m})_\parallel + \frac{i\omega}{\rho}\mathcal{T}_{1\parallel}\,, \tag{33}$$

and

$$-\omega^2 v_y = v_A^2\frac{1}{B^2}(\boldsymbol{B}\cdot\nabla)^2 v_y\,, \tag{34}$$

where quantities with subscripts $n$ and $\parallel$ denote the normal and parallel projections. The first two equations are decoupled from the third one, for they only contain the $v_n$ and $v_\parallel$ components of the velocity, while the other has the $v_y$ component only. One can then consider either a velocity of the form $\boldsymbol{v} = v_y\hat{\boldsymbol{e}}_y$ and solve the $y$-component of the wave equation, or a velocity $\boldsymbol{v} = v_n\hat{\boldsymbol{e}}_n + v_\parallel\hat{\boldsymbol{e}}_\parallel$ and solve equations (32) and (33). Equation (34) is the equation of the Alfvén mode, driven solely by the magnetic tension and having associated no plasma pressure or magnetic pressure variations (eqs. [27] and [28] have no $v_y$ component.) On the other hand, equations (32) and (33) are the equations of magnetoacoustic modes, whose restoring forces are the gradient of the total (gas + magnetic) pressure and the magnetic tension.

Let us now calculate the perturbed flux function for the magnetoacoustic modes. Expression $\nabla\cdot\boldsymbol{B}_1 = 0$ allows one to write the perturbation to the magnetic field as $\boldsymbol{B}_1 = \nabla\times\boldsymbol{A}_1$. This, together with the induction equation (16), implies

$$\boldsymbol{A}_1 = \frac{1}{i\omega}\boldsymbol{v}\times\boldsymbol{B}\,. \tag{35}$$

Taking into account that $B_{1y} = 0$ for magnetoacoustic modes, $\boldsymbol{A}_1$ can be cast as $\boldsymbol{A}_1 = A_1\hat{\boldsymbol{e}}_y$, with

$$A_1 = -\frac{1}{i\omega}Bv_n\,. \tag{36}$$

And not surprisingly, only displacements normal to field lines can disturb their shape.

### 2.3. *Line-tied Alfvén and Slow Continuous Spectra*

The physical nature of the Alfvén continuous spectrum is clearly shown by equation (34), which tells us that the information on the oscillatory state of any plasma element can only be transmitted along magnetic field lines. The impossibility of communicating that state across magnetic surfaces implies that every magnetic surface oscillates independently of the others, with its own set of frequencies (determined by the physical properties of that particular surface). Changing smoothly the considered surface produces a continuous variation of that set of frequencies (hence the term *continuous spectrum* is given to this part of the spectrum).

On a magnetic surface, the flux function remains constant, which, from equation (6), implies that the coordinates $x$ and $z$ are no longer independent. Denoting by $x = x_0$ the position of the footpoint of a field line ($z = 0$), we have

$$\cos kx_0 = \cos kxe^{-lz}\,, \qquad A = \text{const}\,. \tag{37}$$

It must be noted that $A = \text{const}$ on a magnetic surface implies $B_x = \text{const}$.

© American Astronomical Society • Provided by the NASA Astrophysics Data System

1996ApJ...461..4240



Thus, the derivative $\boldsymbol{B} \cdot \nabla$ along field lines can be expressed as

$$\boldsymbol{B} \cdot \nabla = B_x \frac{d}{dx}, \qquad A = \text{const}, \tag{38}$$

and equation (34) reduces to an ordinary differential equation,

$$\frac{d^2 v_y}{dx^2} + \frac{B^2}{B_x^2} \frac{\omega^2}{v_A^2} v_y = 0, \qquad A = \text{const}. \tag{39}$$

We assume that the photosphere ($z = 0$) behaves as a rigid and perfectly conducting medium to coronal perturbations so that the boundary conditions become

$$v_y(\pm x_0) = 0. \tag{40}$$

Equations (39) and (40) then constitute an eigenvalue problem for the eigenfunction $v_y(x)$ and the eigenvalue $\omega$.

The existence of the slow continuum is not so apparent from equations (32) and (33). One can obtain the expression describing the slow continuum following Poedts & Goossens (1991), who gave a general derivation of the slow and Alfvén continuum equations in a two-dimensional equilibrium without gravity. For our particular equilibrium, their general formulae reduce to equation (34) for the Alfvén continuum and

$$\frac{c_s^2}{B^2} (\boldsymbol{B} \cdot \nabla) \left[ \frac{v_A^2}{c_s^2 + v_A^2} (\boldsymbol{B} \cdot \nabla) \frac{v_\parallel}{B} \right] + \omega^2 \frac{v_\parallel}{B} = 0, \qquad A = \text{const} \tag{41}$$

for the slow continuum.

An alternative derivation of this expression can be made by attending to the physical nature of the modes in the continuum. Some authors (e.g., Goedbloed 1983; Mond, Hameiri, & Hu 1990; Thompson & Wright 1993) have shown that the velocity components are characterized by a strong divergence in the neighborhood of the singular surface. We then assume $(\nabla A \cdot \nabla) v_n \gg (\boldsymbol{B} \cdot \nabla) v_n$, $(\nabla A \cdot \nabla) v_n \gg v_n$ and $(\nabla A \cdot \nabla) f v_n \simeq f (\nabla A \cdot \nabla) v_n$, with $f$ any combination of equilibrium quantities (and similarly for $v_\parallel$). In addition, it is found that the parallel ($v_\parallel$) and perpendicular ($v_y$) components are more singular than the normal ($v_n$) component, and so we require $v_\parallel \gg v_n$. After using these assumptions, equations (32) and (33) reduce to

$$(\nabla A \cdot \nabla) \left[ (c_s^2 + v_A^2)(\nabla A \cdot \nabla) v_n + c_s^2 B (\boldsymbol{B} \cdot \nabla) \frac{v_\parallel}{B} \right] \simeq 0 \tag{42}$$

and

$$c_s^2 \frac{1}{B} (\boldsymbol{B} \cdot \nabla) \left[ \frac{1}{B} (\nabla A \cdot \nabla) v_n + (\boldsymbol{B} \cdot \nabla) \frac{v_\parallel}{B} \right] \simeq -\omega^2 v_\parallel. \tag{43}$$

Now, equation (42) tells us that the derivative across a magnetic surface of a quantity made up of the sum of two divergent terms vanishes, which implies that the term inside the square brackets in this equation has to be zero. This allows one to express $(\nabla A \cdot \nabla) v_n$ in terms of $v_\parallel$,

$$(\nabla A \cdot \nabla) v_n \simeq -\frac{c_s^2}{c_s^2 + v_A^2} B (\boldsymbol{B} \cdot \nabla) \frac{v_\parallel}{B}. \tag{44}$$

Finally, after inserting this expression into equation (43), equation (41) is obtained.

Equation (38) is now used to express the directional derivative as a derivative with respect to $x$ within a magnetic surface, so that

$$\frac{d}{dx} \left( \frac{v_A^2}{c_s^2 + v_A^2} \frac{d}{dx} \frac{v_\parallel}{B} \right) + \frac{B^2}{B_x^2} \frac{\omega^2}{c_s^2} \frac{v_\parallel}{B} = 0, \qquad A = \text{const}. \tag{45}$$

This ordinary differential equation is supplemented by the boundary conditions

$$v_\parallel(\pm x_0) = 0. \tag{46}$$

Eigensolutions belonging to the continuum part of the spectrum present a singular behavior in the neighborhood of a given field line. In the previous treatment of the continuum, the singular part has been removed from the solutions and equations (39) and (45) apply only to the regular part of the eigenmodes on the singular magnetic surface. This is the reason why the original partial differential equations reduce to ordinary differential equations with no singularities.

## 3. MAGNETOACOUSTIC MODES: NUMERICAL METHOD AND BOUNDARY CONDITIONS

This section is devoted to the description of the numerical procedure used in solving equations (32) and (33). They are two partial differential equations (PDEs) in two dimensions with the unknowns $v_n$, $v_\parallel$ and the eigenvalue $\omega$. In what follows, the code developed to perform the integration of these equations is simply referred to as "the numerical code."

© American Astronomical Society • Provided by the NASA Astrophysics Data System

1996ApJ...461..4240



### 3.1. *General $\psi, \chi$ Coordinates*

The derivatives of the velocity components in equations (32) and (33) have been written as combinations of the operators $\nabla A \cdot \nabla$ and $\boldsymbol{B} \cdot \nabla$. For the numerical integration of the wave equations, it will be necessary to write these operators explicitly in terms of partial derivatives in the directions defined by two spatial coordinates, for which the names $\psi$ and $\chi$ are used, which are functions of $x$ and $z$ and map the part of the $x$-$z$ plane in which the numerical solution is to be computed.

A simple choice of coordinates $\psi, \chi$ is

$$\psi = z/L\,, \qquad 0 \le \psi \le H/L\,, \tag{47}$$

$$\chi = x/L\,, \qquad -1 \le \chi \le 1\,, \tag{48}$$

with $2L$ the lateral extent of the arcade. This corresponds to a system whose height is limited to the maximum value $z = H$. It may be convenient to use these coordinates with large values of the parameter $H$ to obtain a qualitative idea of the behavior of the solutions for $H \to \infty$. But it is also possible to define another coordinate system in which the height can increase to infinity so that the magnetoacoustic wave equations are solved on the whole arcade,

$$\psi = \frac{1}{z/L + 1}\,, \qquad 0 \le \psi \le 1\,, \tag{49}$$

$$\chi = x/L\,, \qquad -1 \le \chi \le 1\,. \tag{50}$$

A third pair of coordinates are the flux coordinates

$$\psi = \cos\, kxe^{-lz}\,, \qquad 0 \le \psi \le 1\,, \tag{51}$$

and

$$\chi = \frac{\sin\, kxe^{-lz}}{(1 - \psi^2)^{1/2}}\,, \qquad -1 \le \chi \le 1\,. \tag{52}$$

With these coordinates, field lines become straight lines with $\psi = \text{const}$ and, for each value of $\psi$, $\chi$ varies between $-1$ and 1, which means all magnetic field lines have a length of two units in this coordinate system. The normalization of the length of all field lines to the same value is achieved by the factor $(1 - \psi^2)^{1/2}$ in the denominator of equation (52), while the inclusion of sin $kx$ in the numerator ensures independence of the coordinates $\psi$ and $\chi$. The photosphere ($z = 0$) corresponds to $\chi = 1$ for $0 \le x \le 1$ and to $\chi = -1$ for $-1 \le x \le 0$. The line $\psi = 0$ corresponds to the field line going from the bottom left corner of the arcade ($x = -L$, $z = 0$), up to infinity and then down to the bottom right corner ($x = L$, $z = 0$), so that the whole $x$-$z$ plane is enclosed in a rectangular box (see Fig. 1*c*). This line comprises three of the four arcade boundaries in the $x$-$z$ plane: the two lateral vertical lines at $x = \pm L$ and the one at $z \to \infty$. The $\psi = 1$ line also deserves some attention, since it corresponds to the point $x = 0$, $z = 0$, that is, to the top of a field line touching the photosphere at a single point.

One can think of the transformation of these field-related coordinates back to Cartesian coordinates by bending up field lines and moving the photosphere in such a way that the two points $\psi = 1$, $\chi = -1$ and $\psi = 1$, $\chi = 1$ are brought together and the lines $\chi = -1$ and $\chi = 1$ form a horizontal, straight line. After this process, one recovers the configuration shown in Figure 1*a*, with the field line $\psi = 0$ giving rise to the outermost arcade field line.

### 3.2. *Solving the Magnetoacoustic Wave Equations by Finite Differences*

One can now write the operators $\nabla A \cdot \nabla$, $\boldsymbol{B} \cdot \nabla$, $(\nabla A \cdot \nabla)^2$, etc., in equations (32) and (33) in terms of the general coordinates $\psi$ and $\chi$ (see Appendix B). The resulting expressions can be cast as

$$a_{11}\frac{\partial^2 v_n}{\partial \psi^2} + b_{11}\frac{\partial^2 v_n}{\partial \psi\, \partial \chi} + c_{11}\frac{\partial^2 v_n}{\partial \chi^2} + d_{11}\frac{\partial v_n}{\partial \psi} + e_{11}\frac{\partial v_n}{\partial \chi} + f_{11}\, v_n + a_{12}\frac{\partial^2 v_\parallel}{\partial \psi^2} + b_{12}\frac{\partial^2 v_\parallel}{\partial \psi\, \partial \chi} + c_{12}\frac{\partial^2 v_\parallel}{\partial \chi^2}$$
$$+ d_{12}\frac{\partial v_\parallel}{\partial \psi} + e_{12}\frac{\partial v_\parallel}{\partial \chi} + f_{12}\, v_\parallel = \omega^2 v_n\,, \tag{53}$$

$$a_{21}\frac{\partial^2 v_n}{\partial \psi^2} + b_{21}\frac{\partial^2 v_n}{\partial \psi\, \partial \chi} + c_{21}\frac{\partial^2 v_n}{\partial \chi^2} + d_{21}\frac{\partial v_n}{\partial \psi} + e_{21}\frac{\partial v_n}{\partial \chi} + f_{21}\, v_n + a_{22}\frac{\partial^2 v_\parallel}{\partial \psi^2} + b_{22}\frac{\partial^2 v_\parallel}{\partial \psi\, \partial \chi} + c_{22}\frac{\partial^2 v_\parallel}{\partial \chi^2}$$
$$+ d_{22}\frac{\partial v_\parallel}{\partial \psi} + e_{22}\frac{\partial v_\parallel}{\partial \chi} + f_{22}\, v_\parallel = \omega^2 v_\parallel\,. \tag{54}$$

The expressions for the nonconstant coefficients $a_{11}$, $b_{11}$, etc., are given in Appendix C.

We now construct a finite difference replacement of equations (53) and (54). The region to be considered is a rectangle with sides parallel to the $\psi$- and $\chi$-axes, covered by a mesh of $N_\psi \times N_\chi$ points in which approximations to the functions $v_n$ and $v_\parallel$ are to be computed. At the point $(\psi_i, \chi_j)$, the first and second derivatives of these functions are approximated in the usual manner (Mitchell & Griffiths 1980; Ames 1992; Allen, Herrera, & Pinder 1988):

$$\left.\frac{\partial v_n}{\partial \psi}\right|_{i,j} = \frac{v_n^{(i+1,j)} - v_n^{(i-1,j)}}{2h_\psi} + O(h_\psi^2)\,, \tag{55}$$

© American Astronomical Society • Provided by the NASA Astrophysics Data System

1996ApJ...461..4240



$$\left.\frac{\partial v_n}{\partial \chi}\right|_{i,j} = \frac{v_n^{(i,j+1)} - v_n^{(i,j-1)}}{2h_\chi} + O(h_\chi^2) , \tag{56}$$

$$\left.\frac{\partial^2 v_n}{\partial \psi^2}\right|_{i,j} = \frac{v_n^{(i+1,j)} - 2v_n^{(i,j)} + v_n^{(i-1,j)}}{h_\psi^2} + O(h_\psi^2) , \tag{57}$$

$$\left.\frac{\partial^2 v_n}{\partial \chi^2}\right|_{i,j} = \frac{v_n^{(i,j+1)} - 2v_n^{(i,j)} + v_n^{(i,j-1)}}{h_\chi^2} + O(h_\chi^2) , \tag{58}$$

and similarly for $v_\parallel$. In these expressions, $v_n^{(i,j)}$ is the value of $v_n$ at the point $(\psi_i, \chi_j)$, and $h_\psi$, $h_\chi$ are the uniform grid spacings in the $\psi$- and $\chi$-directions. For the mixed derivative, one has (see Mitchell & Griffiths 1980)

$$\left.\frac{\partial^2 v_n}{\partial \psi\, \partial \chi}\right|_{i,j} = \frac{1}{h_\psi h_\chi}\{(\alpha_2 - \alpha_1)[v_n^{(i+1,j)} + v_n^{(i,j+1)} + v_n^{(i-1,j)} + v_n^{(i,j-1)} - 2v_n^{(i,j)}]$$
$$+ \alpha_1[v_n^{(i+1,j+1)} + v_n^{(i-1,j-1)}] - \alpha_2[v_n^{(i-1,j+1)} + v_n^{(i+1,j-1)}]\} + O[\max(h_\psi^2, h_\chi^2)] . \tag{59}$$

The parameters $\alpha_1$ and $\alpha_2$ in this expression can be chosen so as to minimize the error of the difference approximation. This results in the formula

$$\alpha_1 + \alpha_2 = \tfrac{1}{2} . \tag{60}$$

Equation (59) as it stands makes use of the function whose derivative is being approximated at nine points. Setting $\alpha_1 = \frac{1}{2}$, $\alpha_2 = 0$ or $\alpha_1 = 0$, $\alpha_2 = \frac{1}{2}$ has the effect of reducing the number of points to just seven, while taking $\alpha_1 = \alpha_2 = \frac{1}{4}$ results in only four points being used. The freedom in the selection of one of the quantities $\alpha_1$, $\alpha_2$ can be used to improve the stability and convergence of the numerical solution. It is worth noticing that they can both be changed from one point to another and/or have different values for the approximation of the mixed derivatives of $v_n$ and $v_\parallel$.

Using expressions (55)–(59) to discretize equations (53) and (54) in the $(N_\psi - 2) \times (N_\chi - 2)$ interior points yields $2(N_\psi - 2)(N_\chi - 2)$ equations for the unknowns at the interior points and $2(N_\psi + N_\chi - 2)$ unknowns at the points on the boundary of the system. The same discretized equations can be assumed to apply at the boundary points, but then some boundary conditions on $v_n$ and $v_\parallel$ are needed to eliminate the unknowns that are introduced by the use of points outside the region of integration. This issue will be discussed next.

### 3.3. *Boundary Conditions*

We start with the boundary conditions at the base of the arcade. As has been already mentioned, the photospheric influence on coronal disturbances, i.e., the line-tying effect, is modeled by rigid wall conditions. Hence,

$$v_n = v_\parallel = 0 , \qquad z = 0 . \tag{61}$$

Let us now consider the upper boundary. In an arcade limited to a maximum height $H$, some field lines traverse this horizontal boundary. We think of them as being anchored at that position, and so we require the vanishing of $v_n$ and $v_\parallel$ there. When the whole arcade is considered, the upper boundary is placed at an infinite height, and all perturbations are assumed to go to zero as $z \to \infty$. Then,

$$v_n = v_\parallel = 0 , \qquad z = H \text{ or } z \to \infty . \tag{62}$$

Finally, we have to deal with the two lateral boundaries. We assume that, when set into motion, the plasma does not traverse those boundaries, which implies that normal motions cannot occur there, although parallel motions are still possible. An inspection of the particular form of equations (53) and (54) at $x = \pm L$ reveals that, upon using $v_n = 0$, they are only consistent with $\partial v_\parallel / \partial x = 0$, so we require

$$v_n = \frac{\partial v_\parallel}{\partial x} = 0 , \qquad x = \pm L . \tag{63}$$

In view of the three conditions (61)–(63) and from the numerical viewpoint, there are two types of boundary: those at which both $v_n$ and $v_\parallel$ must vanish and those where $v_n$ and the derivative of $v_\parallel$ normal to the boundary are zero. The first case is the simplest to treat, and one only needs to consider the finite difference equivalent to equations (53) and (54) at interior points while taking $v_n$ and $v_\parallel$ equal to zero. This does not introduce any extra unknowns.

The second case is a bit more difficult to handle, since the use of the difference equations at boundary points implies introducing fictitious points exterior to the region of integration. The boundary condition on $v_\parallel$ allows one to eliminate the value of this function on the exterior points by approximating the normal derivative by centered differences (eq. [56]). Then there remains the problem of the values of $v_n$ on the fictitious points, for the condition on this variable just tells us that it vanishes on the boundary. We have studied equations (53) and (54) at $x = \pm L$, and it is possible to conclude that $\partial^2 v_n / \partial^2 x = 0$ on this boundary. This allows one to express the value of $v_n$ outside the rectangle as minus the value of $v_n$ directly across the boundary.

With the use of any of the three coordinate systems described above, the boundary of the integration domain is rectangular, and the treatment of boundary conditions is the same for all of them. It is only necessary to translate the $x$-derivative in equation (63) to a derivative with respect to one of the general coordinates $\psi$ and $\chi$, which can be done easily for all three

© American Astronomical Society • Provided by the NASA Astrophysics Data System

1996ApJ...461..424O

coordinate systems used in this paper. To sum up, we have a grid made of the interior points plus the points on those boundaries at which $v_n$ and $v_\parallel$ do not vanish simultaneously. We denote by $N$ the total number of points.

### 3.4. *Solving the Eigenvalue Problem*

The points on the two-dimensional grid are now ordered consecutively, and each of them is given a number between 1 and $N$. Next, the unknowns are put together in a single vector $\boldsymbol{U}$ constructed as follows:

$$\boldsymbol{U} = (v_n^1, v_\parallel^1, v_n^2, v_\parallel^2, \ldots, v_n^N, v_\parallel^N)^T , \tag{64}$$

where $v_n^k$ and $v_\parallel^k$, $k = 1, 2, \ldots, N$, stand for the approximate values of the eigenfunctions $v_n$ and $v_\parallel$ at the $k$th grid point. The discrete approximation to equations (53) and (54) is then an algebraic eigenvalue problem,

$$\boldsymbol{AU} = \lambda \boldsymbol{U} , \tag{65}$$

with $\boldsymbol{A}$ a large, sparse, nonsymmetric matrix, and

$$\lambda = \omega^2 . \tag{66}$$

This eigenvalue problem has been solved using an inverse vector iteration algorithm, which allows one to compute a single eigensolution at a time and is much faster than calculating all eigenvalues of $\boldsymbol{A}$ (e.g., Kerner 1989). Next, the technique is described briefly. Given an approximation $\lambda_0$ to the required eigenvalue $\lambda$, the vector $\lambda_0 \boldsymbol{x}$ (with $\boldsymbol{x} \equiv \boldsymbol{U}$) is subtracted from both sides of equation (65), which reduces to

$$(\boldsymbol{A} - \lambda_0 \boldsymbol{I})\boldsymbol{x} = \Delta\lambda \boldsymbol{x} , \tag{67}$$

with $\Delta\lambda$ such that

$$\lambda = \lambda_0 + \Delta\lambda . \tag{68}$$

The eigenvector $\boldsymbol{x}$ and $\Delta\lambda$ are then computed as the iterative solution to the system

$$(\boldsymbol{A} - \lambda_0 \boldsymbol{I})\boldsymbol{x}_i = \Delta\lambda_{i-1} \boldsymbol{x}_{i-1} , \qquad i = 1, 2, 3, \ldots , \tag{69}$$

with $\Delta\lambda_i$ given by the Rayleigh quotient

$$\Delta\lambda_i = \frac{\boldsymbol{x}_i^T(\boldsymbol{A} - \lambda_0 \boldsymbol{I})\boldsymbol{x}_i}{\boldsymbol{x}_i^T \boldsymbol{x}_i} , \qquad i = 1, 2, 3, \ldots . \tag{70}$$

The iterative process proceeds as follows: an initial vector $\boldsymbol{x}_0$, which can be simply filled with random numbers, and an initial value $\Delta\lambda_0$, for which we take $\lambda_0 \times 10^{-4}$, are given and the solution $\boldsymbol{x}_1$ to the set of linear equations (69) with $i = 1$ is computed. Then the correction $\Delta\lambda_1$ is obtained from equation (70), and we are ready to start the second iteration. The process is successfully halted when $\Delta\lambda$ converges.

To improve the accuracy of the solution for a nonsymmetric matrix $\boldsymbol{A}$, it is convenient to construct a second sequence of iterative solutions based on the left-hand eigenvectors $\boldsymbol{y}$, which satisfy

$$\boldsymbol{A}^T \boldsymbol{y} = \lambda \boldsymbol{y} . \tag{71}$$

An expression similar to equation (69) can now be constructed as before,

$$(\boldsymbol{A} - \lambda_0 \boldsymbol{I})^T \boldsymbol{y}_i = \Delta\lambda_{i-1} \boldsymbol{y}_{i-1}, \qquad i = 1, 2, 3, \ldots , \tag{72}$$

and the quantity $\Delta\lambda_i$ is computed by means of the generalized Rayleigh quotient,

$$\Delta\lambda_i = \frac{\boldsymbol{y}_i^T(\boldsymbol{A} - \lambda_0 \boldsymbol{I})\boldsymbol{x}_i}{\boldsymbol{y}_i^T \boldsymbol{x}_i} , \qquad i = 1, 2, 3, \ldots . \tag{73}$$

The final scheme is based on equations (69), (72), and (73), which are solved iteratively until the solution converges.

The task of solving equations (69) and (72) can be performed with standard routines that utilize the sparseness of the matrix $\boldsymbol{A}$, such as the NAG routines F01BRF, F01BSF, and F04AXF, or the Harwell routine library MA28.

Before determining some specific eigensolutions of the system, we first compute the whole eigenspectrum of the matrix $\boldsymbol{A}$ using a coarse grid. We use a numerical routine that calculates all eigenvectors and eigenvalues of a real, unsymmetric matrix, such as the NAG subroutine F02AGF. We then have a rough idea of the features of the spectrum and can concentrate on calculating particular eigensolutions with more grid points and, therefore, with higher accuracy.

### 3.5. *Computation of the Perturbed Forces*

After solving the eigenvalue problem, equation (65), we have an approximation to the spatial distribution of the functions $v_n$ and $v_\parallel$ from which the perturbed quantities (plasma pressure, magnetic pressure, magnetic field, density) and perturbed forces (pressure gradient, magnetic pressure gradient, and magnetic tension) can be obtained. We use equations (14) and (24)–(29) and again write the directional derivatives as in Appendix B and approximate the derivatives of $v_n$ and $v_\parallel$ in the resulting expressions by the finite difference formulae (55)–(59). We have found it very useful to compute these physical quantities, mainly the perturbed forces, for they are the drivers of the oscillatory motions and are ultimately responsible for the nature of the modes.

© American Astronomical Society • Provided by the NASA Astrophysics Data System

1996ApJ...461..4240



## 4. RESULTS: ALFVÉN AND SLOW CONTINUOUS SPECTRA

The differential equations governing the spatial variation of $v_y$ and $v_{\|}$ within a singular magnetic surface have been given in § 2.3. Those equations are valid for a two-dimensional equilibrium with any temperature profile, no gravity, and no component of the magnetic field in the ignorable direction. The results presented in this section assume a uniform temperature distribution. Equation (39) for Alfvén modes then can be written as

$$\frac{d^2 v_y}{dx^2} + \frac{\omega^2}{v_{Ax}^2} v_y = 0 , \qquad A = \text{const} , \tag{74}$$

where $v_{Ax}^2 = B_x^2/(\mu\rho)$ is

$$v_{Ax}^2 = \frac{2c_s^2}{\gamma} \frac{(l^2/k^2)\cos^2 kx_0}{[1-(l^2/k^2)]\cos^2 kx_0 + \beta_0} , \qquad A = \text{const} . \tag{75}$$

The above equation has solution

$$v_y(x) = C \sin \frac{n\pi}{2x_0}(x + x_0) , \tag{76}$$

with $C$ an arbitrary integration constant and $n = 1, 2, \ldots$. The solution has been written in such a way that it already satisfies the line-tying boundary condition (40) at $x = -x_0$. The frequency $\omega(x_0)$ is obtained after imposing the other boundary condition and is given by

$$\omega^2 = \left(\frac{n\pi}{2x_0}\right)^2 \frac{2c_s^2}{\gamma} \frac{(l^2/k^2)\cos^2 kx_0}{[1-(l^2/k^2)]\cos^2 kx_0 + \beta_0} . \tag{77}$$

This expression can also be cast in the more familiar form

$$\omega^2 = k_x^2 v_{Ax}^2 , \tag{78}$$

with

$$k_x = \frac{n\pi}{2x_0} , \qquad n = 1, 2, \ldots . \tag{79}$$

Equations (76) and (77) show that for a fixed value of $x_0$, i.e., for a given field line, there corresponds a set of eigensolutions and eigenfrequencies. As we mentioned above, varying $x_0$ has the effect of changing the set of frequencies associated with the particular field line. This can be seen in Figure 2*a*, where values of $n$ up to 10 have been used. For a given $n$, oscillations of field lines close to the arcade boundary ($x_0/L$ close to 1) have small frequencies, whereas oscillations of field lines near the point $x = 0$, $z = 0$ (with $x_0/L$ close to 0) have much larger values of $\omega$. This is a consequence of the difference in the lenghts of field lines for different values of $x_0$: since the period can be considered as roughly twice the time it takes for a wave to travel back and forth along the field line, longer lines have higher oscillatory periods.

Consider now Figure 2*a* and Figure 2*a* of Oliver et al. (1993), obtained for a potential equilibrium with uniform density. The similarity of the frequency variation with the singular magnetic surface in both figures is noticeable. To ascertain the influence that nonpotentiality has on $\omega$, we consider $n = 1$ in equation (77) and plot the frequency for different values of the parameters $\beta_0$ and $l/k$ (see Fig. 2*b*). In the potential case, the first term in the denominator of equation (77) vanishes, and the frequency becomes inversely proportional to the square root of $\beta_0$. Thus, a change in the background pressure has a great impact on the

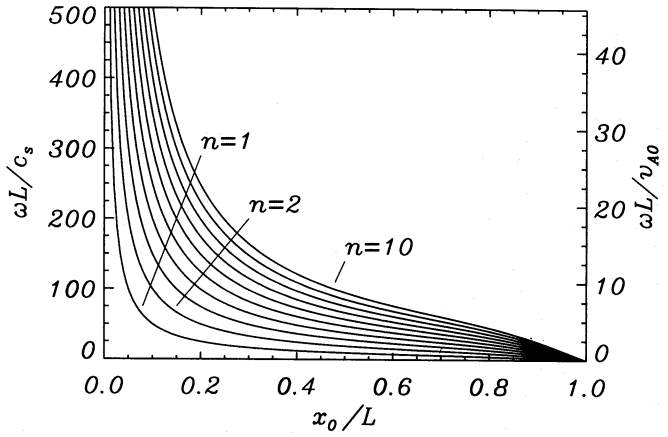


FIG. 2*a*

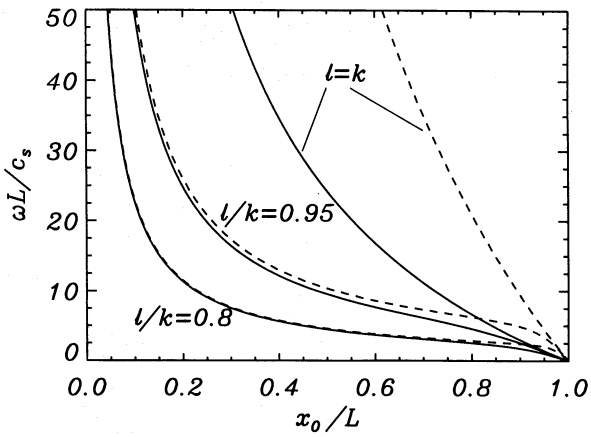


FIG. 2*b*

FIG. 2.—(*a*) Frequency of Alfvén continuum modes vs. the footpoint position $x_0$ of magnetic field lines for $\beta_0 = 10^{-2}$, $l/k = 0.95$. Only the fundamental mode and first few harmonics are plotted. The right vertical axis gives $\omega$ nondimensionalized against $v_{A0}/L$, where we have set $v_{A0}^2 \equiv v_A^2(\pm L, 0) = 2c_s^2/(\gamma\beta_0)$. (*b*) Frequency of the Alfvén continuum fundamental mode for the values $l/k = 1$, $l/k = 0.95$, and $l/k = 0.8$. *Solid lines*: $\beta_0 = 10^{-2}$. *Dashed lines*: $\beta_0 = 10^{-3}$.

© American Astronomical Society • Provided by the NASA Astrophysics Data System

1996ApJ...461..4240



$\omega$ of the potential solution. However, as $l/k$ departs from unity, the term with the factor $(1 - l^2/k^2)$ becomes more important and is everywhere much bigger than $\beta_0$, except near the arcade boundary where the cosine becomes zero. Hence, the similarity between the solid and dashed bottom curves ($l/k = 0.8$) in Figure 2*b*. The influence of $l/k$ on the frequency is also quite noticeable (compare all three solid lines or all three dashed lines in Fig. 2*b*). Two different effects produce these variations of the frequency, namely, the modification of the equilibrium magnetic field and the change in the density, generated by the coupling of the plasma pressure to the magnetic field. The first one is responsible for the factor $l^2/k^2$ in equation (77). It turns out, however, that the magnetic structures of both equilibria differ very little, and the largest influence to the frequency comes from the density, which depends here on the field line considered, while in the potential arcade a uniform density has been used.

Next we turn our attention to the slow mode continuum (eqs. [45] and [46]). The ordinary differential equation has been solved numerically for $c_s = \text{const}$ (uniform temperature), and the frequency and parallel velocity have been obtained at given magnetic surfaces. Figure 3*a* is a plot of $\omega$ versus the footpoint position $x_0$ for $\beta_0 = 10^{-2}$ and $l/k = 0.95$. The shape of the curves in this plot is similar to the shape of the curves in Figure 2*a*. However, the typical speeds of propagation of slow and Alfvén modes ($c_s$ and $v_A$) take very different values in the corona, which yields quite distinct frequency ranges for these modes.

Figure 3*b* shows the frequency of the fundamental slow continuum mode for various values of $l/k$. Changing $\beta_0$ between $10^{-3}$ and $10^{-2}$ does not produce any important variation in $\omega$, and so a fixed value of this parameter has been used to compute the results shown in this figure. The parameter $l/k$ has a larger influence on $\omega$, although this effect is smaller than that found when discussing Alfvén modes. Let us assume that the Alfvén speed is much larger than the sound speed, which is usually true, and let us approximate $c_s^2 + v_A^2$ by $v_A^2$. Then equation (45) reduces to

$$\frac{d^2}{dx^2}\frac{v_\parallel}{B} + \frac{B^2}{B_x^2}\frac{\omega^2}{c_s^2}\frac{v_\parallel}{B} = 0\,, \tag{80}$$

where

$$\frac{B^2}{B_x^2} = \frac{1}{(l^2/k^2)\cos^2 kx} + \left(1 - \frac{k^2}{l^2}\right), \qquad A = \text{const}\,. \tag{81}$$

The solutions obtained by solving equation (80) have frequencies close to the ones computed before (and plotted in Fig. 3*b*), and so it constitutes a good approximation to equation (45). The absence of $\beta_0$ in it is an explanation for the scarce influence that this parameter has on $\omega$. Moreover, the factor $B^2/B_x^2$ makes the frequency depend entirely on the magnetic field structure, which does not change very much for the values of $l/k$ used in Figure 3*b*, hence the minor influence of this quantity on the frequency.

### 4.1. *Check of the Numerical Code: Slow Continuum Solutions*

The performance of the two-dimensional code (numerical stability, convergence, etc.) has been checked for a simpler equilibrium than the one used in this paper and will be described elsewhere. A proof of the reliability of the numerical code can also be obtained by a comparison with the results given in the previous section. There the properties of the slow continuum modes were determined by solving equation (45) on different magnetic surfaces. We now reproduce those results by solving the discretized two-dimensional equations (32) and (33) in the coordinate system related to the magnetic field (given by eqs. [51] and [52]). The advantage of such a coordinate system is that the lines of constant $\psi$ coincide with field lines, and so the regular behavior of continuum solutions on a particular field line can be obtained more easily.

Two-dimensional solutions are computed for $\beta_0 = 10^{-2}$, $l/k = 0.95$ with the numerical code. All solutions found have $v_\parallel \neq 0$ on a given magnetic surface and $v_\parallel = 0$ on all other magnetic surfaces, while $v_n$ vanishes everywhere. This is explained by the absence of dissipation in our problem and by the spatial discretization used, which imply that our numerical code is not

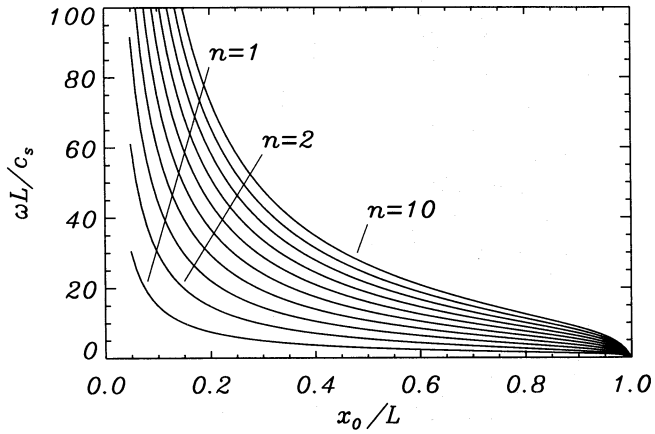


FIG. 3*a*

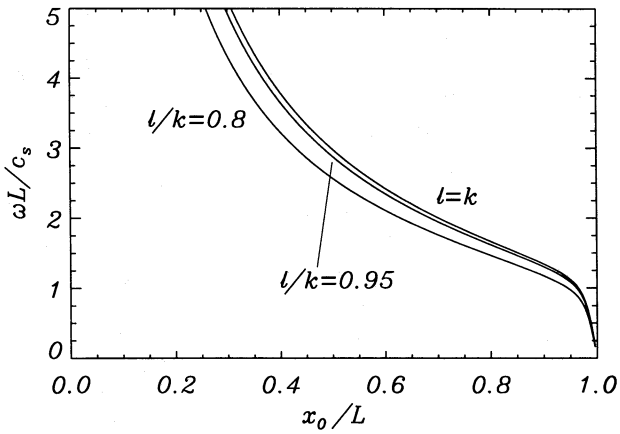


FIG. 3*b*

FIG. 3.—(*a*) Frequency of slow continuum modes vs. the footpoint position $x_0$ of magnetic field lines for $\beta_0 = 10^{-2}$, $l/k = 0.95$. Only the fundamental mode and first few harmonics are plotted, for $0.05 \leq x_0 \leq 0.99$. (*b*) Frequency of the slow continuum fundamental mode for $\beta_0 = 10^{-2}$ and the parameter values $l = k$ (potential arcade), $l/k = 0.95$, and $l/k = 0.8$.

© American Astronomical Society • Provided by the NASA Astrophysics Data System

1996ApJ...461..4240



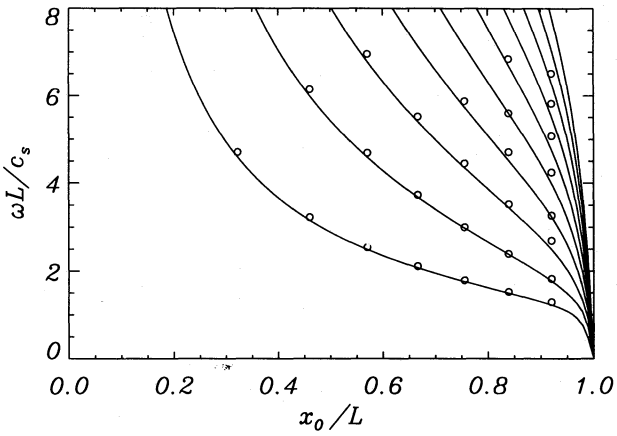


FIG. 4a

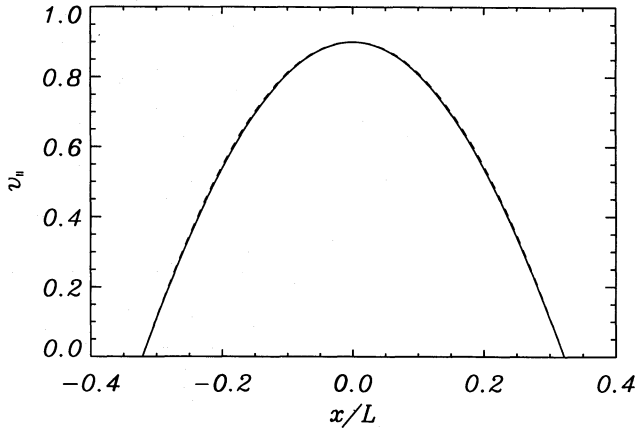


FIG. 4b

FIG. 4.—(*a*) Comparison of slow continuum frequencies obtained solving eq. (45) (*solid lines*) and solving the full-wave eqs. (32) and (33) with the two-dimensional numerical code (*open circles*). The parameter values are the ones used to produce Fig. 3*a*. (*b*) Spatial profile of the parallel velocity of the fundamental slow continuum mode ($x_0 \simeq 0.32$). The solid line is the solution to eq. (45), and the dashed line is the finite difference solution to eqs. (32) and (33) on the singular surface. This eigenfunction, whose amplitude is given in arbitrary units, is associated to the leftmost circle in (4*a*).

capable of picking up the singular part of the solution and that only the regular part can be obtained. To check that the numerical solutions are really continuum solutions, one can compare their frequencies and the $x$-dependence of the parallel component of the velocity with the ones obtained by integrating equation (45). In Figure 4*a* we have plotted the lower part of Figure 3*a* (with $\omega L/c_s < 8$) and have superimposed the discrete values of the frequency obtained with the two-dimensional numerical code. The agreement is surprisingly good for the small number of grid points used in the numerical computations ($N_\psi = 9$ and $N_\chi = 40$). Omitting the field lines corresponding to $\psi = 0$ and $\psi = 1$, the value $N_\psi = 9$ allows one to obtain $\omega$ on seven field lines (that is, seven values of $x_0$), hence the arrangement of the circles on seven vertical lines. A similar comparison can also be made for the variation of $v_{\parallel}$ on the singular surface (see Fig. 4*b*). After normalizing the two solutions so that their maxima coincide, the agreement is again excellent.

## 5. RESULTS: MAGNETOACOUSTIC MODES

The results presented in this section have been obtained with the coordinate systems given by equations (47)–(48), for $H$ finite, and equations (49)–(50), for infinite $H$. The computations presented below are all done for $H = L$ unless stated otherwise.

### 5.1. *Potential Coronal Arcade*

The study of the magnetoacoustic normal modes of coronal arcades is begun with the potential state ($l = k$). It has already been mentioned that this problem was investigated by Oliver et al. (1993) in the limit of vanishing plasma $\beta$. If one wants to recover the results obtained in that work, it is now necessary to *turn off* the perturbed pressure gradient terms in equations (32) and (33). This, together with $\nabla^2 A = 0$ for $l = k$, results in the function $v_{\parallel}$ being zero everywhere and all oscillatory motions taking place in the direction normal to the field lines. Of the two partial differential equations (PDEs) (53) and (54), only the first one has to be solved, since the coefficients of the second are all zero.

The numerical code is used as described in § 3.2 (i.e., the two PDEs are solved) to study the properties of fast modes in this situation, in which they are not coupled to slow modes. Under these conditions, the coefficients of the wave equations are independent of the parameter $\beta_0$, whose value does not influence the results. The computations yield $\omega$ and $v_n$ at the grid points together with the eigenfunction $v_{\parallel}$, which is zero everywhere within the limits of machine precision. The frequencies thus obtained have been plotted, together with the values computed as in Oliver et al. (1993) (see Fig. 5), which are more accurate than the present work since they are obtained with high precision by solving a dispersion relation. The agreement between the two sets of solutions is better for low-$\omega$ modes, having only a few spatial oscillations in the domain of solution. This is a common feature of finite difference approximations when solving eigenvalue problems, namely, the fact that the smoother the spatial variation of the actual eigenfunction, the better the accuracy of the numerical solution (as an example, see Mitchell & Griffiths 1980, pp. 161–163). An obvious check of the convergence of the results is to increase the number of grid points in the difference approximation: the accuracy of the numerical solutions then improves, and the values of $\omega$ become closer to the "exact" ones.

Regarding the spatial profile of the normal velocity component, it really appears to be a separable function of the $x$ and $z$ variables, as was assumed in Oliver et al. (1993) to obtain analytical solutions to the wave equation. Regions of positive/negative $v_n$ are separated by straight lines parallel to the $x$- and $z$-axes. These types of solutions are qualitatively similar to those of a vibrating rectangular drum in which nodal lines are parallel to the edges of the membrane.

When keeping the pressure gradient term in the wave equations, fast and slow modes are present and coupled to each other, a coupling that becomes greater as the plasma $\beta$ is increased. Actually, for $\beta_0 = 10^{-2}$ and $l/k = 0.95$ (which gives $\beta \approx 0.33$ at a height $z = L$), the coupling of the two magnetoacoustic modes is so strong that it is impossible to talk of fast and slow modes as such. The magnetoacoustic modes in this "high" $\beta$ configuration display a mixture of the properties of fast and slow

© American Astronomical Society • Provided by the NASA Astrophysics Data System

1996ApJ...461..424O



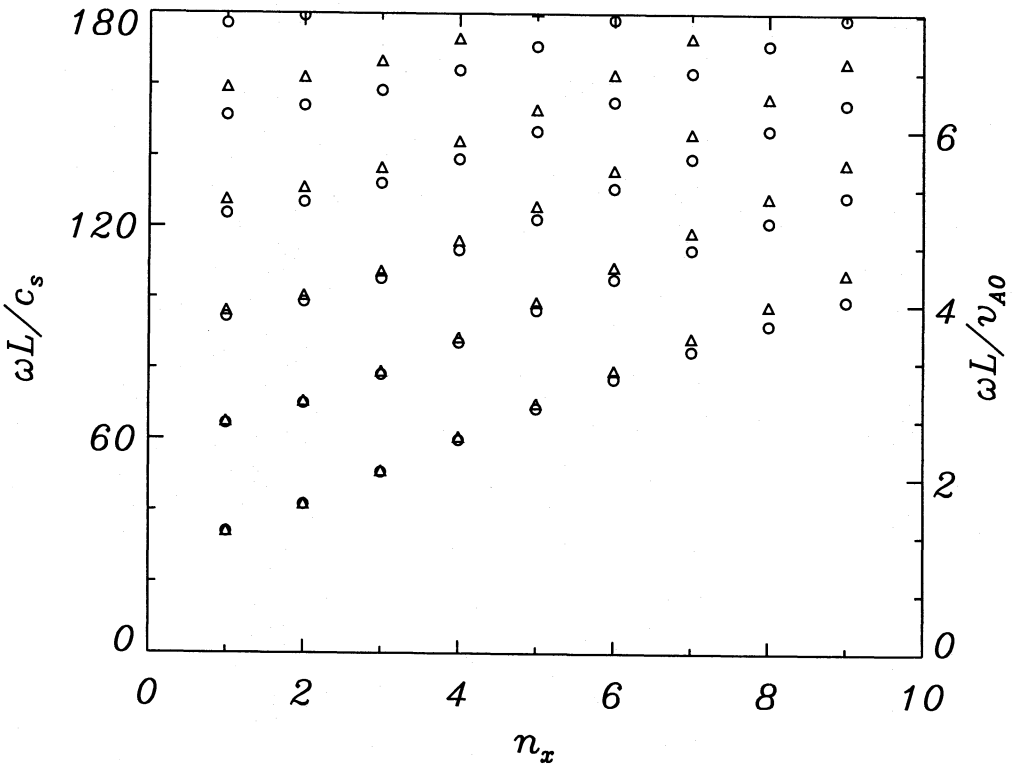


FIG. 5.—Comparison of fast-mode frequencies in the limit $\beta = 0$, $l = k$ (potential magnetic configuration). Triangles represent $\omega$ computed as in Oliver et al. (1993). Circles represent $\omega$ computed numerically by solving the coupled eqs. (32) and (33) with 20 grid points in each spatial direction ($N_x = N_z = 20$). The number of nodes of the eigenvector $v_n$ in the $x$-direction is $n_x + 1$. For a given $n_x$ and with increasing $\omega$, the number of nodes $n_z + 1$ of $v_n$ in the vertical direction is 2, 3, ....

modes. Even for lower values of the parameter $\beta_0$, fast and slow modes do not exist as *pure* modes. However, there are modes with a predominantly "slow" character and modes with a predominantly "fast" character, which we will call slow and fast. The distinctive properties of the two magnetoacoustic modes are studied in the next section for a nonpotential configuration.

Let us comment very briefly on the changes produced by the pressure terms on fast modes. After retaining $\nabla p_1$ in these equations $v_\parallel$ is no longer zero, although its amplitude is very small compared to that of $v_n$, which means that fast modes drive motions predominantly normal to the magnetic field. Moreover, the inclusion of pressure forces has little influence on $v_n$ or on the frequency of the modes, which remain mostly unchanged. A contour plot of the normal velocity component, Figure 6*a*, shows that it still possesses nodal lines parallel to the $x$- and $z$-axes.

### 5.2. *Nonpotential Coronal Arcade*

Unless otherwise stated, in this section we use the values $\beta_0 = 2 \times 10^{-3}$ and $l/k = 0.95$.

As before, pressure terms are first eliminated in the differential equations so as to exclude slow modes and to be able to investigate pure fast modes. Now, for $l \neq k$ the quantity $\nabla^2 A$ does not vanish and the perturbed magnetic force has a net component in the parallel direction. Hence, a property of the nonpotential structure is that magnetic forces are capable of

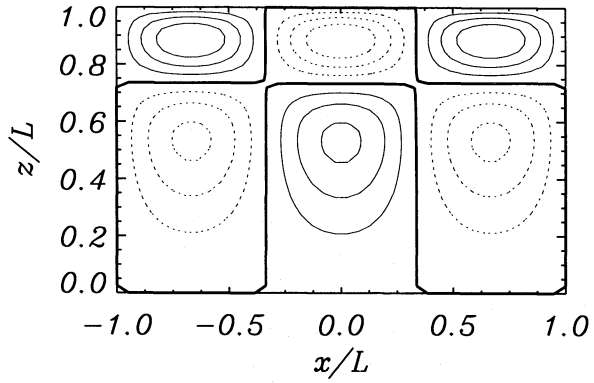


FIG. 6*a*

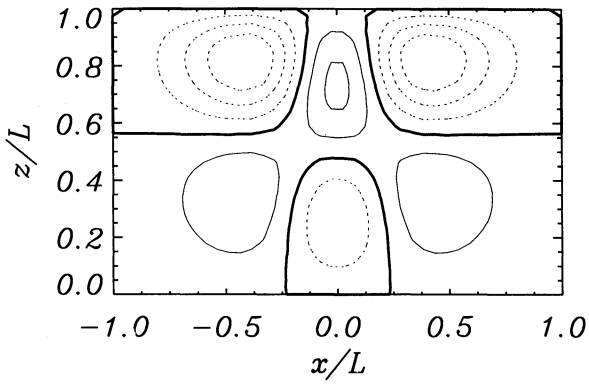


FIG. 6*b*

FIG. 6.—Contour plot of the normal velocity component of a fast-mode harmonic for $\beta_0 = 2 \times 10^{-3}$ and (*a*) $l/k = 1$ (potential equilibrium) and (*b*) $l/k = 0.95$ (nonpotential equilibrium). Thick solid lines give the level of zero $v_n$, while thin solid lines and dashed lines give levels of equispaced positive/negative $v_n$. The numerical integration of the wave equations has been performed with $N_x = N_z = 40$.

© American Astronomical Society • Provided by the NASA Astrophysics Data System

1996ApJ...461..4240



driving not only normal motions, but also motions parallel to the magnetic field. Another important difference between the present configuration and the potential one is the big change in the frequency of fast modes (by a factor of 3 for the fundamental mode). This is more striking when one realizes that the spatial variation of the component $v_n$ is similar in both cases. In addition, the other features of fast modes that were described in the previous section are also characteristic of the fast modes for $l \neq k$: the domain of integration is divided in quasi-rectangular regions of alternate positive and negative $v_n$, and the maxima of this velocity component always appear in the upper part of the arcade.

Fast modes are characterized not only as being driven by the perturbed Lorentz force, but also as having $v_n \gg v_{\parallel}$, simply because the perturbed force is directed almost in the normal direction. When only magnetic forces drive motions of the plasma, the amplitude of the normal velocity component is between 1 and 2 orders of magnitude larger than the amplitude of the parallel component. We will show later that the pressure gradient term generates large $v_{\parallel}$ and that some fast modes are found for which $v_n < v_{\parallel}$ holds.

Now that we know the main properties of fast modes, the effects of plasma pressure are retained in equations (32) and (33), which are solved as they stand. One expects the two magnetoacoustic modes to have oscillatory frequencies in different ranges of $\omega$, since their characteristic speeds of propagation ($c_s$ and $v_A$) are of very different magnitude for the values of the plasma $\beta$ considered here. Indeed, when solving the full wave equations, we find eigensolutions with $\omega$ well below those found above with no pressure term, and so we think of these modes as slow-mode candidates. To confirm this suspicion, it is necessary to investigate their physical nature and the forces that drive the motions.

Let us consider the mode with the smallest frequency. The normal components of the perturbed pressure and the perturbed magnetic Lorentz force are spatially out of phase and almost counteract each other. This implies that motions driven in the normal direction possess small amplitudes. On the other hand, the parallel component of the pressure force is much larger than the parallel component of the magnetic term. Then, the total force is dominated by the parallel component, which takes values 2 orders of magnitude larger than the normal one, thus yielding a $v_{\parallel}$ that dominates over $v_n$. Figure 7 is a two-dimensional vector plot of the velocity $\boldsymbol{v} = v_n \hat{\boldsymbol{e}}_n + v_{\parallel} \hat{\boldsymbol{e}}_{\parallel}$ showing the fact that motions take place along field lines. This figure displays another distinctive feature, namely, the strong anisotropy of the motions, which occur in a region given by a group of neighboring magnetic field lines.

Summarizing, the most important properties of this mode are that it is driven basically by the pressure gradient force, which produces parallel motions; that pressure and magnetic forces act spatially out of phase in the normal direction; and that the importance of the related motions is linked to the shape of magnetic field lines. The first property is also a well-known feature of slow modes propagating in an infinite medium. The third one is obviously related to the fact that slow modes propagate better along field lines than across them. We then refer to modes with the above properties as slow modes.

Let us consider the slow-mode harmonics. They have frequencies above the fundamental (which means that the slow-mode spectrum is a *Sturmian* one), and their spatial variation is more complicated than that of the fundamental mode. But this does not come as a surprise, for one expects more and more spatial oscillations of the solution as higher harmonics are considered. However, the manner in which these oscillations occur is somewhat unsuspected. We show this point with the help of some

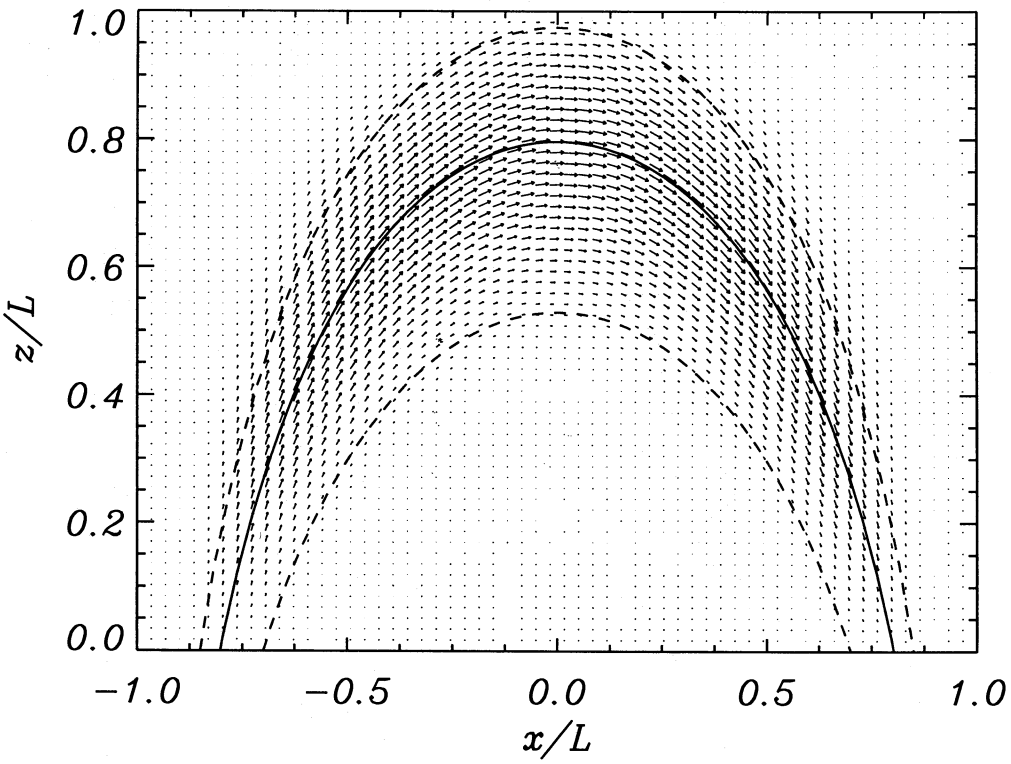


FIG. 7.—Vector field plot of the total velocity (normal + parallel components) for the fundamental slow mode ($l/k = 0.95$, $\beta_0 = 2 \times 10^{-3}$). Field lines passing through the maximum of the velocity (*solid*) and some other field lines (*dashed*) have been superimposed to show the polarization of motions in the parallel direction. The numerical integration of the wave equations has been performed with $N_x = N_z = 60$.

© American Astronomical Society • Provided by the NASA Astrophysics Data System

1996ApJ...461..439



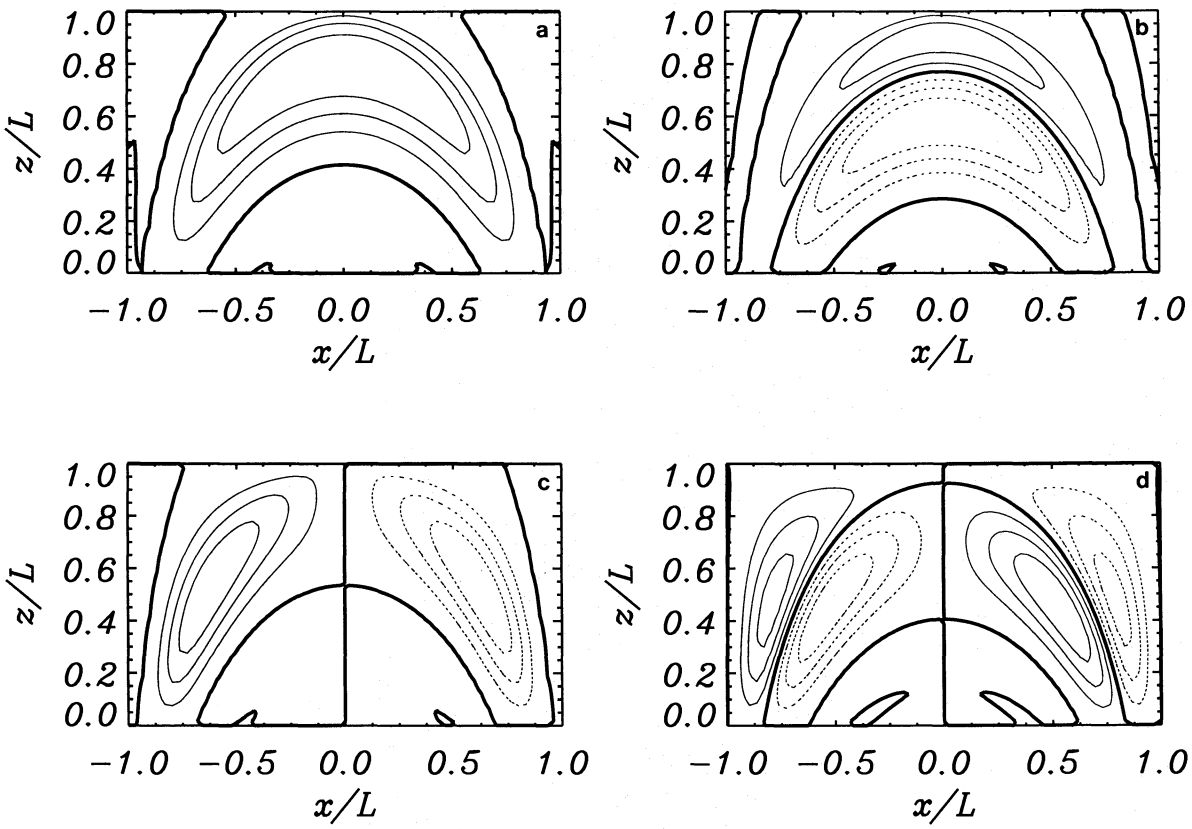


FIG. 8.—Contour plot of the parallel velocity component of some slow modes showing the change in the spatial structuring of the solution ($l/k = 0.95$ and $\beta_0 = 2 \times 10^{-3}$). (*a*) Fundamental mode ($\omega L/c_s = 1.74$). (*b*) First harmonic ($\omega L/c_s = 2.01$). (*c*) Fourth harmonic ($\omega L/c_s = 2.71$). (*d*) Sixth harmonic ($\omega L/c_s = 3.06$). The numerical integration of the wave equations has been performed with $N_x = N_z = 60$.

contour plots of the parallel velocity for various modes (Fig. 8). (We do not consider the normal component, since it is always negligible compared to $v_{\|}$.) Each mode is characterized by the number $n_1$ of regions or *banana-like* bands of nonzero $v_{\|}$ centered around preferred field lines and the number $n_2$ of *semioscillations* taking place within each of these regions. Therefore, the fundamental mode has $n_1 = 1$, $n_2 = 1$ (Fig. 8*a*), the first harmonic has $n_1 = 2$, $n_2 = 1$ (see Fig. 8*b*), the fourth harmonic is an $n_1 = 1$, $n_2 = 2$ mode (Fig. 8*c*), the harmonic shown in Figure 8*d* is an $n_1 = 2$, $n_2 = 2$ mode, etc. These two numbers then give a means of classifying slow modes (Fig. 9*a*).

The main problem we face when considering fast modes is the very strong interaction between the magnetic Lorentz force and the pressure gradient. This interaction also exists for slow modes, for which the normal component of the two forces counteract each other. Moreover, the parallel component of slow modes is dominated by the pressure term, and so displace-

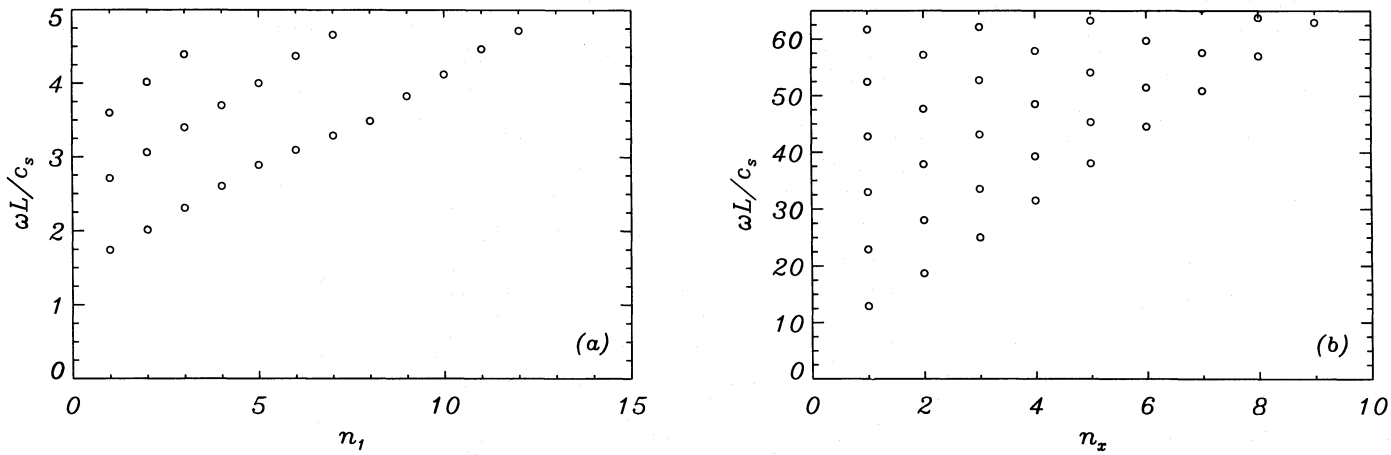


FIG. 9.—Slow- and fast-mode dispersion diagrams computed for $l/k = 0.95$ and $\beta_0 = 2 \times 10^{-3}$. (*a*) Dimensionless frequency $\omega L/c_s$ of slow modes plotted vs. the number $n_1$ of oscillations of $v_{\|}$ across field lines. For each given value of $n_1$, the number $n_2$ of oscillations of $v_{\|}$ along field lines is 1, 2, 3, . . . . Solutions have been computed individually using the inverse vector iteration, and 60 grid points have been taken in each direction ($N_x = N_z = 60$). (*b*) Dimensionless fast-mode frequency vs. the number $n_x$ of oscillations of $v_n$ in the horizontal direction. For each given value of $n_x$, the number $n_z$ of oscillations of $v_n$ in the vertical direction is 1, 2, 3, . . . . The solutions have been computed by solving the full eigensystem with $N_x = N_z = 20$.

© American Astronomical Society • Provided by the NASA Astrophysics Data System

1996ApJ...461..440



ments in this direction are preferred. Nevertheless, the situation changes for fast modes and, although the perturbed magnetic term is usually larger than the pressure term, these two forces are of the same order of magnitude. This means that, in the present configuration, fast modes are not driven solely by magnetic forces, but also by pressure forces.

For the parameter values considered here ($\beta_0 = 2 \times 10^{-3}$ and $l/k = 0.95$), the frequency of the fundamental fast mode is a factor of 10 larger than the frequency of the fundamental slow mode, which has a noticeable effect on the perturbed pressure force. To explain this point, let us go back to the slow modes. It has been shown that the larger the frequency of a slow-mode harmonic, the more spatial oscillations has the solution and, because slow modes are driven by the perturbed pressure force, this implies that the pressure force develops more and more spatial structuring as the frequency is increased. As the frequency increases to reach that of the fundamental fast mode, the pressure term has already developed a rapidly oscillating spatial structuring. As a consequence of the coupling between forces in the momentum equation, the magnetic force also has a strong spatial structuring.

The spatial distribution of the function $v_n$ still maintains some similarity with that of the eigensolutions of the vibrating membrane (compare Figs. 6*a* and 6*b*), although the coupling to slow modes can be seen to produce a deformation that tends to follow field lines. The other properties of fast modes found in the limiting cases $l = k$ and $\nabla p_1 = 0$, however, have now been destroyed by the interaction of magnetic and pressure forces: the normal velocity component is usually larger than $v_{\|}$ by a factor of 2 at the maximum (and not by a factor of 10 or 100 as before), and normal motions are not solely driven by the magnetic Lorentz force.

The spectrum of fast modes is *Sturmian* (Fig. 9*b*) and does not suffer big changes in its appearance, except for a factor of 3 change in frequency, when compared to the spectrum of pure fast modes in a potential arcade (Fig. 5).

Finally, we want to make a brief comment on the existence of a certain symmetry in the solutions about $x = 0$. This fact can be anticipated from the form of the equilibrium equations (6)–(9) and the symmetry of the imposed boundary conditions about the plane $x = 0$. All the results presented in this section display this symmetry of the eigenfunctions about the $z$-axis (see Figs. 6, 7, and 8). A saving in the computer time needed can be achieved by using the range $0 \leq x \leq 1$ and imposing the boundary conditions deriving from parity considerations on $v_n$ and $v_{\|}$ at $x = 0$.

## 6. CONCLUSIONS

A magnetic arcade configuration in which the pressure gradient counteracts the magnetic Lorentz force has been considered. In deriving the equilibrium equations, two restrictive assumptions have been made: the magnetic field in the $y$-direction has been eliminated, and gravity has been excluded. However, it may not be justified to use these approximations in the structures under study. On the one hand, horizontal photospheric motions can give rise to displacements of the footpoints of magnetic field lines that would result in a shearing of the whole magnetic structure. On the other hand, gravitational forces are of great importance in a plasma when the height of the system is much smaller than the temperature scale height divided by the plasma beta. The effect of eliminating gravity and the sheared magnetic field component in the force balance equation can be quite important, and they should be included in future studies of this kind. However, it must be taken into account that with this work we do not pretend to study a totally sound arcade equilibrium, but to investigate the basic features of the MHD modes of oscillation characteristic of the solar corona, which has led us to simplify the equilibrium so that the different forces that drive the vibratory motions and their interaction have been kept as simple as possible without losing much physical information. Below we mention the influence of gravity and the longitudinal magnetic field component on the wave equations. Let us just mention that the generalization of the present configuration to one with $B_y \neq 0$, $\boldsymbol{g} \neq 0$ is straightforward in the isothermal case and has already been done analytically by Zweibel & Hundhausen (1982).

In the derivation of the equations of MHD adiabatic waves, a general two-dimensional equilibrium configuration has been assumed with $B_y = 0$ and $\boldsymbol{g} = 0$, instead of using the explicit equations for the equilibrium parameters given in § 2.1. In this manner, we obtain a description of the MHD oscillations of the system that is valid for a wide class of equilibria. The final equations depend on the derivatives along and across field lines of $p$ and $B$ (the quantities $p_a$, $p_s$, $B_a$, etc.), which are the only calculations required for any equilibrium.

The decomposition of the different vectors (velocity, perturbed magnetic field, magnetic tension, magnetic pressure gradient, pressure gradient, and momentum equation) in their components has also been performed in a general manner by projecting them onto field-related directions. Then the expressions for the driving forces $\nabla p_1$, $\nabla p_{1m}$, and $\mathcal{T}_1$ have been obtained and substituted into the momentum equation. The outcome is a set of three equations in terms of the normal, parallel, and perpendicular components of the oscillatory velocity. Of these three equations, which determine the Alfvén, fast, and slow modes of the system, one is decoupled from the other two: it is the equation for Alfvén modes and involves motions in the $y$-direction, driven only by the magnetic tension and generating no pressure perturbations. The other two equations govern the fast and slow magnetoacoustic modes and are, in general, quite complicated in a two-dimensional configuration, including the arcade equilibrium studied in this paper, so we have proceeded to their solution by numerical means. The reason for the decoupling of Alfvén modes from the two magnetoacoustic modes is that the equilibrium magnetic field is shearless and waves have been assumed not to propagate along the arcade main axis. Had we taken $B_y \neq 0$ or $\partial/\partial y \neq 0$, the three wave equations would have been coupled together, which complicates the physical nature of the modes enormously. Had gravity been included, its effect would not be so drastic, since it would merely give rise to some extra terms in the momentum equations that would act as "pollutants" of the main driving forces.

Alfvén and slow continuum solutions, characterized by nonsquare integrable eigenfunctions on given magnetic surfaces, have been computed. It is found that the frequency of these modes decreases as longer field lines, close to the arcade's lateral boundary, are considered. Clearly, waves are restricted by means of the photospheric line tying to travel back and forth within a given magnetic surface, and so longer field lines imply larger travel times and smaller frequencies. A second-order effect is the change of the effective propagation speed of the waves within magnetic surfaces, which makes $\omega$ not inversely proportion-

© American Astronomical Society • Provided by the NASA Astrophysics Data System

1996ApJ...461..4240



al to the length of field lines, as the previous statement would imply. The influence of nonpotentiality on the continuum modes has also been investigated by comparison with the results in Oliver et al. (1993). The main result is that Alfvén modes are the most affected by changes in the equilibrium because the Alfvén speed is modified while the sound speed is not. The small variations of the frequency of slow modes with the parameters of the equilibrium (Fig. 3*b*) can be ascribed to the change in the magnetic configuration, which is reflected automatically in the continuum modes.

Applications of continuum modes in the context of solar coronal arcades and loops can be found in Poedts & Goossens (1987, 1988, 1991). Of these works, the first two are of particular interest here since the magnetic field is unsheared, as in the present case; the equilibrium consists of a coronal arcade or loop with elliptical magnetic field lines embedded in a nonuniform plasma. A comparison between their results and ours is difficult because of the intrinsic difference in the equilibrium structure. Consider, for example, Figure 8 in Poedts & Goossens (1991), which shows the nonsingular spatial variation of the Alfvén mode eigenfunction $\xi_y$ (similar to our $v_y$). Because of the nonuniformity of the equilibrium density within magnetic surfaces, the amplitude of the eigenfunction is larger at the top of the loop than at the feet. However, Alfvén mode eigenfunctions found here possess a constant amplitude (see eq. [76]) as a result of the uniform equilibrium density along magnetic field lines. In addition, the frequency spectra display some differences and similarities; consider our Figure 2*b* and Figure 7 in Poedts & Goossens (1991), where the square of the Alfvén continuum frequency is plotted against the flux function $\psi$. Although the variables in the horizontal axes in these figures are not the same, they map different magnetic surfaces in a similar manner, and a comparison can be made. In Figure 2*b*, the frequency decreases as one moves from the center of the arcade toward outer field lines. This is exactly what one finds for $\psi < 1$ in the Poedts & Goossens graph, although the trend is reversed for $\psi > 1$. These and other differences should not be taken as a drawback of these kinds of investigations, but they should rather encourage us to continue studying the modes of coronal structures, whose physical properties could be determined from observed oscillatory properties.

For the solution of the magnetoacoustic mode equations, finite differences have been used. The approach to the problem followed here allows one to use different coordinate systems (e.g., Cartesian or field-aligned), which has allowed us to check the two-dimensional numerical code by recovering the slow continuum eigensolutions. The code solves two partial differential equations supplemented by homogeneous boundary conditions of Dirichlet and Neumann type, with the subsequent solution of the resulting eigenvalue problem using an inverse vector iteration.

Of the two magnetoacoustic modes, only the fast wave survives the elimination of the pressure term from the wave equations. These pure fast modes are shown to have a dominant velocity component normal to the magnetic field (in fact, $v_{\|} = 0$ for a potential equilibrium). Moreover, the spatial structure of $v_n$ is similar to that of a vibrating membrane, as was reported by Oliver et al. (1993), with the nodal lines of $v_n$ dividing the arcade into rectangular regions of alternate positive and negative $v_n$, as a consequence of the isotropic propagation of fast waves. The effect of nonpotentiality on the frequencies of the modes is noticeable and implies a typical reduction by a factor of 3 when compared to those of the potential equilibrium.

The inclusion of the pressure force has a great influence on the modes. First of all, it is not possible to talk of fast and slow waves, although all modes display either a clear slow character or a clear fast character and so we refer to them simply as slow and fast. Photospheric line tying is probably responsible for this situation, and it gives rise to the mixing of the MHD modes in most other configurations (see Goedbloed & Halberstadt 1994 for a particular example). The main effect of the pressure term on fast modes is an increase in the amplitude of parallel motions compared to that of normal motions, which is more important for nonpotential equilibria in which, for many modes, the two velocity components have comparable amplitudes. The spatial variation of $v_n$ is also strongly modified, and the regions of positive and negative $v_n$ are distorted to a shape suggestive of the field line structure (compare Figs. 6*a* and 6*b*). It is then possible to conclude that the interaction with slow modes gives rise to some anisotropy in fast modes. On the other hand, the frequency of fast modes is basically unaffected by pressure effects.

As for slow modes, they share the common feature of giving rise to displacements almost parallel to the magnetic field and of having a strong spatial anisotropy. For all harmonics, it is found that the dominant parallel velocity component displays spatial oscillations across field lines, so that nodal lines of $v_{\|}$ are parallel to $\boldsymbol{B}$, and along field lines. In addition, the normal component of the perturbed pressure gradient and Lorentz force mutually counteract each other, and the parallel component of the pressure term remains as the only driver of the motions.

Equation (36) for the perturbed flux function gives the possibility of addressing the issue of field line bending by the magnetoacoustic modes. In view of the results presented here, one can conclude that slow modes are characterized by little field-line bending, since the amplitude of normal motions they generate is quite small, whereas fast modes are capable of generating larger modifications to the structure of the magnetic field. This is in good agreement with the conclusions of Goedbloed & Halberstadt (1994) for a uniform configuration with straight magnetic field lines and is probably a main feature of fast and slow modes of other systems.

The authors acknowledge financial support received from the Spanish Ministery of Science and Education (grant PB93-0420) and from NATO (grant CRG 901002). R. O. wishes to thank the UK PPARC for a postdoctoral research assistantship.

## APPENDIX A

The gradient of a function $f$ of $x$ and $z$ or of any other pair of coordinates that map the $x$-$z$ plane is given by

$$\nabla f = \frac{1}{B}(\nabla A \cdot \nabla) f \hat{\boldsymbol{e}}_n + \frac{1}{B}(\boldsymbol{B} \cdot \nabla) f \hat{\boldsymbol{e}}_{\|} \,. \tag{A1}$$

© American Astronomical Society • Provided by the NASA Astrophysics Data System

1996ApJ...461..4240



And the divergence of a vector $\boldsymbol{v} = v_n \hat{\boldsymbol{e}}_n + v_\parallel \hat{\boldsymbol{e}}_\parallel + v_y \hat{\boldsymbol{e}}_y$ that depends on the same coordinates is (with $\partial/\partial y = 0$)

$$\nabla \cdot \boldsymbol{v} = \frac{1}{B}(\nabla A \cdot \nabla) v_n + \left(\frac{\nabla^2 A}{B} - B_a\right) v_n + \frac{1}{B}(\boldsymbol{B} \cdot \nabla) v_\parallel - B_s v_\parallel \,. \tag{A2}$$

These two expressions, together with equation (2) and the equality $\nabla A = \hat{\boldsymbol{e}}_y \times \boldsymbol{B}$, are used in deriving equations (24)–(28).

Moreover, the calculation of the perturbed magnetic tension (eq. [29]) requires the derivatives of $\hat{\boldsymbol{e}}_n$ and $\hat{\boldsymbol{e}}_\parallel$ in the directions given by these two vectors, which are

$$(\hat{\boldsymbol{e}}_n \cdot \nabla)\hat{\boldsymbol{e}}_n = B_s \hat{\boldsymbol{e}}_\parallel \,, \tag{A3}$$

$$(\hat{\boldsymbol{e}}_n \cdot \nabla)\hat{\boldsymbol{e}}_\parallel = -B_s \hat{\boldsymbol{e}}_n \,, \tag{A4}$$

$$(\hat{\boldsymbol{e}}_\parallel \cdot \nabla)\hat{\boldsymbol{e}}_n = \left(\frac{\nabla^2 A}{B} - B_a\right)\hat{\boldsymbol{e}}_\parallel \,, \tag{A5}$$

$$(\hat{\boldsymbol{e}}_\parallel \cdot \nabla)\hat{\boldsymbol{e}}_\parallel = -\left(\frac{\nabla^2 A}{B} - B_a\right)\hat{\boldsymbol{e}}_n \,. \tag{A6}$$

In the previous expressions and throughout the paper, the following definitions for the derivatives of the equilibrium magnetic field strength are used:

$$B_a = \frac{1}{B^2}(\nabla A \cdot \nabla) B \,, \tag{A7}$$

$$B_s = \frac{1}{B^2}(\boldsymbol{B} \cdot \nabla) B \,, \tag{A8}$$

$$B_{aa} = \frac{1}{B^3}(\nabla A \cdot \nabla)^2 B \,, \tag{A9}$$

$$B_{as} = \frac{1}{B^3}(\nabla A \cdot \nabla)(\boldsymbol{B} \cdot \nabla) B \,, \tag{A10}$$

$$B_{sa} = \frac{1}{B^3}(\boldsymbol{B} \cdot \nabla)(\nabla A \cdot \nabla) B \,, \tag{A11}$$

$$B_{ss} = \frac{1}{B^3}(\boldsymbol{B} \cdot \nabla)^2 B \,. \tag{A12}$$

Similarly, for the derivatives of the equilibrium pressure we have used the short-hand notation

$$p_a = \frac{1}{B}(\nabla A \cdot \nabla) p \,, \tag{A13}$$

$$p_s = \frac{1}{B}(\boldsymbol{B} \cdot \nabla) p = 0 \,, \tag{A14}$$

$$p_{aa} = \frac{1}{B}(\nabla A \cdot \nabla) p_a \,, \tag{A15}$$

$$p_{as} = \frac{1}{B}(\nabla A \cdot \nabla) p_s = 0 \,, \tag{A16}$$

$$p_{sa} = \frac{1}{B}(\boldsymbol{B} \cdot \nabla) p_a \,, \tag{A17}$$

and

$$p_{ss} = \frac{1}{B}(\boldsymbol{B} \cdot \nabla) p_s = 0 \,. \tag{A18}$$

By virtue of equation (1), the pressure of the gas is uniform on each magnetic surface and the quantities $p_s$, $p_{as}$, and $p_{ss}$ vanish.

## APPENDIX B

In this Appendix the expressions for the directional derivatives, written in terms of $\partial/\partial\psi$ and $\partial/\partial\chi$ [with $\psi = \psi(x, z)$ and $\chi = \chi(x, z)$ a pair of independent coordinates], are given:

$$\frac{1}{B}(\nabla A \cdot \nabla) = \psi_a \frac{\partial}{\partial \psi} + \chi_a \frac{\partial}{\partial \chi} \,, \tag{B1}$$

© American Astronomical Society • Provided by the NASA Astrophysics Data System

1996ApJ...461..424O

$$\frac{1}{B}(\boldsymbol{B}\cdot\nabla) = \psi_s\frac{\partial}{\partial\psi} + \chi_s\frac{\partial}{\partial\chi}, \tag{B2}$$

$$\frac{1}{B^2}(\nabla A\cdot\nabla)^2 = \psi_a^2\frac{\partial^2}{\partial\psi^2} + 2\psi_a\chi_a\frac{\partial^2}{\partial\psi\,\partial\chi} + \chi_a^2\frac{\partial^2}{\partial\chi^2} + \psi_{aa}\frac{\partial}{\partial\psi} + \chi_{aa}\frac{\partial}{\partial\chi}, \tag{B3}$$

$$\frac{1}{B^2}(\nabla A\cdot\nabla)(\boldsymbol{B}\cdot\nabla) = \psi_a\psi_s\frac{\partial^2}{\partial\psi^2} + (\psi_a\chi_s + \psi_s\chi_a)\frac{\partial^2}{\partial\psi\,\partial\chi} + \chi_a\chi_s\frac{\partial^2}{\partial\chi^2} + \psi_{as}\frac{\partial}{\partial\psi} + \chi_{as}\frac{\partial}{\partial\chi}, \tag{B4}$$

$$\frac{1}{B^2}(\boldsymbol{B}\cdot\nabla)(\nabla A\cdot\nabla) = \psi_a\psi_s\frac{\partial^2}{\partial\psi^2} + (\psi_a\chi_s + \psi_s\chi_a)\frac{\partial^2}{\partial\psi\,\partial\chi} + \chi_a\chi_s\frac{\partial^2}{\partial\chi^2} + \psi_{sa}\frac{\partial}{\partial\psi} + \chi_{sa}\frac{\partial}{\partial\chi}, \tag{B5}$$

$$\frac{1}{B^2}(\boldsymbol{B}\cdot\nabla)^2 = \psi_s^2\frac{\partial^2}{\partial\psi^2} + 2\psi_s\chi_s\frac{\partial^2}{\partial\psi\,\partial\chi} + \chi_s^2\frac{\partial^2}{\partial\chi^2} + \psi_{ss}\frac{\partial}{\partial\psi} + \chi_{ss}\frac{\partial}{\partial\chi}. \tag{B6}$$

In deriving equations (B3)–(B6), it has been assumed that the mixed derivatives $\partial^2/\partial\psi\,\partial\chi$ and $\partial^2/\partial\chi\,\partial\psi$ of the velocity components $v_n$ and $v_\parallel$ are equal.

The quantities $\psi_a$, $\psi_s$, etc., have been defined as

$$\psi_a = \frac{1}{B}(\nabla A\cdot\nabla)\psi, \tag{B7}$$

$$\psi_s = \frac{1}{B}(\boldsymbol{B}\cdot\nabla)\psi, \tag{B8}$$

$$\psi_{aa} = \frac{1}{B^2}(\nabla A\cdot\nabla)^2\psi, \tag{B9}$$

$$\psi_{as} = \frac{1}{B^2}(\nabla A\cdot\nabla)(\boldsymbol{B}\cdot\nabla)\psi, \tag{B10}$$

$$\psi_{sa} = \frac{1}{B^2}(\boldsymbol{B}\cdot\nabla)(\nabla A\cdot\nabla)\psi, \tag{B11}$$

$$\psi_{ss} = \frac{1}{B^2}(\boldsymbol{B}\cdot\nabla)^2\psi, \tag{B12}$$

and similarly for the derivatives of $\chi$.

## APPENDIX C

The expressions for the coefficients in equations (53) and (54) are given in this Appendix. They have been obtained by gathering together the terms coming from the perturbed total pressure gradient and the perturbed tension in equations (32) and (33).

$$a_{11} = -c_s^2\psi_a^2 - v_A^2(\psi_a^2 + \psi_s^2), \tag{C1}$$

$$b_{11} = -2c_s^2\psi_a\chi_a - 2v_A^2(\psi_a\chi_a + \psi_s\chi_s), \tag{C2}$$

$$c_{11} = -c_s^2\chi_a^2 - v_A^2(\chi_a^2 + \chi_s^2), \tag{C3}$$

$$d_{11} = -\left[(\gamma+1)\frac{p_a}{\rho} + c_s^2\left(\frac{\nabla^2 A}{B} - 2B_a\right)\right]\psi_a - c_s^2\psi_{aa} - v_A^2\left(2\frac{\nabla^2 A}{B}\psi_a + \psi_{aa} + \psi_{ss}\right), \tag{C4}$$

$$e_{11} = -\left[(\gamma+1)\frac{p_a}{\rho} + c_s^2\left(\frac{\nabla^2 A}{B} - 2B_a\right)\right]\chi_a - c_s^2\chi_{aa} - v_A^2\left(2\frac{\nabla^2 A}{B}\chi_a + \chi_{aa} + \chi_{ss}\right), \tag{C5}$$

$$f_{11} = -\left[\frac{p_{aa}}{\rho} + \frac{\gamma p_a}{\rho}\left(\frac{\nabla^2 A}{B} - B_a\right) + c_s^2\frac{1}{B}(\nabla A\cdot\nabla)\left(\frac{\nabla^2 A}{B} - B_a\right)\right] - v_A^2\left[B_{aa} + 2\left(\frac{\nabla^2 A}{B} - B_a\right)B_a + B_{ss} - 2B_s^2\right], \tag{C6}$$

$$a_{12} = -c_s^2\psi_a\psi_s, \tag{C7}$$

$$b_{12} = -c_s^2(\psi_a\chi_s + \psi_s\chi_a), \tag{C8}$$

$$c_{12} = -c_s^2\chi_a\chi_s, \tag{C9}$$

© American Astronomical Society • Provided by the NASA Astrophysics Data System

1996ApJ...461..4240

$$d_{12} = \left(c_s^2 B_a - \frac{\gamma p_a}{\rho}\right)\psi_s + c_s^2 B_s \psi_a - c_s^2 \psi_{as} , \tag{C10}$$

$$e_{12} = \left(c_s^2 B_a - \frac{\gamma p_a}{\rho}\right)\chi_s + c_s^2 B_s \chi_a - c_s^2 \chi_{as} , \tag{C11}$$

$$f_{12} = \frac{\gamma p_a}{\rho} B_s + c_s^2 (B_{as} - 2B_a B_s) , \tag{C12}$$

$$a_{21} = a_{12} , \tag{C13}$$

$$b_{21} = b_{12} , \tag{C14}$$

$$c_{21} = c_{12} , \tag{C15}$$

$$d_{21} = -\frac{p_a}{\rho}\psi_s + c_s^2 B_s \psi_a - c_s^2\left(\frac{\nabla^2 A}{B} - B_a\right)\psi_s - c_s^2 \psi_{sa} - v_A^2 \frac{\nabla^2 A}{B}\psi_s , \tag{C16}$$

$$e_{21} = -\frac{p_a}{\rho}\chi_s + c_s^2 B_s \chi_a - c_s^2\left(\frac{\nabla^2 A}{B} - B_a\right)\chi_s - c_s^2 \chi_{sa} - v_A^2 \frac{\nabla^2 A}{B}\chi_s , \tag{C17}$$

$$f_{21} = -\frac{p_{sa}}{\rho} - c_s^2 \frac{1}{B}(\boldsymbol{B}\cdot\nabla)\left(\frac{\nabla^2 A}{B} - B_a\right) - v_A^2 \frac{\nabla^2 A}{B} B_s , \tag{C18}$$

$$a_{22} = -c_s^2 \psi_s^2 , \tag{C19}$$

$$b_{22} = -2c_s^2 \psi_s \chi_s , \tag{C20}$$

$$c_{22} = -c_s^2 \chi_s^2 , \tag{C21}$$

$$d_{22} = 2c_s^2 B_s \psi_s - c_s^2 \psi_{ss} , \tag{C22}$$

$$e_{22} = 2c_s^2 B_s \chi_s - c_s^2 \chi_{ss} , \tag{C23}$$

$$f_{22} = c_s^2 (B_{ss} - 2B_s^2) . \tag{C24}$$

## REFERENCES


Acton, L., et al. 1992, Science, 258, 618
Allen, M. B., Herrera, I., & Pinder, G. F. 1988, Numerical Modelling in Science and Engineering (New York: John Wiley & Sons)
Ames, W. F. 1992, Numerical Methods for Partial Differential Equations (3d ed.; New York: Academic)
Einaudi, G., & Van Hoven, G. 1981, Phys. Fluids, 24, 1092
Goedbloed, J. P. 1975, Phys. Fluids, 18, 1258
———. 1983, Lecture Notes on Ideal Magnetohydrodynamics (Rijnhuizen Report 83-145, Nieuwegein, The Netherlands)
Goedbloed, J. P., & Halberstadt, G. 1994, A&A, 286, 275
Goossens, M. 1991, in Advances in Solar System Magnetohydrodynamics, ed. E. R. Priest & A. W. Hood (Cambridge: Cambridge Univ. Press), 137
Kerner, W. 1989, J. Comput. Phys., 85, 1
Kuperus, M., & Raadu, M. A. 1974, A&A, 31, 189
Mitchell, A. R., & Griffiths, D. F. 1980, The Finite Difference Method in Partial Differential Equations (New York: John Wiley & Sons)
Mond, M., Hameiri, E., & Hu, P. H. 1990, J. Geophys. Res., 95, 89
Oliver, R., Ballester, J. L., Hood, A. W., & Priest, E. R. 1993, A&A, 273, 647
Poedts, S., & Goossens, M. 1987, Sol. Phys., 109, 265
———. 1988, A&A, 198, 331
———. 1991, Sol. Phys., 133, 281
Priest, E. R. 1988, ApJ, 328, 848
Roberts, B. 1985, in Solar System Magnetic Fields, ed. E. R. Priest (Dordrecht: Kluwer), 37
———. 1991, in Advances in Solar System Magnetohydrodynamics, ed. E. R. Priest & A. W. Hood (Cambridge: Cambridge Univ. Press), 105
Rosner, R., Low, B. C., & Holzer, T. E. 1986, in Physics of the Sun, Vol. II, ed. P. A. Sturrock (Dordrecht: Reidel), 135
Thompson, M. J., & Wright, A. N. 1993, J. Geophys. Res., 98, 15541
Van der Linden, R. A. M., Hood, A. W., & Goedbloed, J. P. 1994, Sol. Phys., 154, 69
Zweibel, E. G., & Hundhausen, A. J. 1982, Sol. Phys., 76, 261


© American Astronomical Society • Provided by the NASA Astrophysics Data System